Chapter 7

MONOTONIC BEHAVIOR

In this chapter we discuss the monotonic strengthening and fracture mechanisms of continuous fiber and discontinuously reinforced metal matrix composites. Cyclic fatigue and creep of MMCs are discussed in chapters 8 and 9, respectively.

7.1 STRENGTHENING MECHANISMS

The monotonic strength and stiffness of MMCs is usually much higher than that of the unreinforced metal. Figure 7.1 shows a general schematic of the evolution of damage in a MMC during monotonic loading. Since the reinforcing phase typically is much stiffer than the matrix, a significant fraction of the stress is initially borne by the reinforcement. Microplasticity then takes place, at a fairly low stress, which corresponds to the original deviation from linearity in the stress-strain curve. This point is termed the proportional limit stress. Microplasticity in the composites has been attributed to stress concentrations in the matrix at the sharp ends of fibers, whiskers, and particles; or at the poles of the reinforcement (Goodier, 1933; Corbin and Wilkinson, 1994; Chawla et al., 1998b; Chawla et al., 2003). With increasing strain, microplasticity increases in magnitude to global plasticity in the matrix. The incorporation of reinforcement results in an increase in work hardening rate of the material, relative to the unreinforced matrix. The higher observed work hardening rate, relative to the unreinforced material, is a simple function of lower matrix volume (by incorporation of the reinforcement), and not necessarily due to a change in work hardening mechanisms. When the matrix is significantly work hardened, the matrix is placed under great constraint (i.e., a triaxial tensile stress develops) with an inability for strain relaxation to take place. This causes the onset of void nucleation and propagation, which take place at a lower far field applied strain than that observed in the unreinforced material. With the onset of void growth in the matrix, the stress in the reinforcement
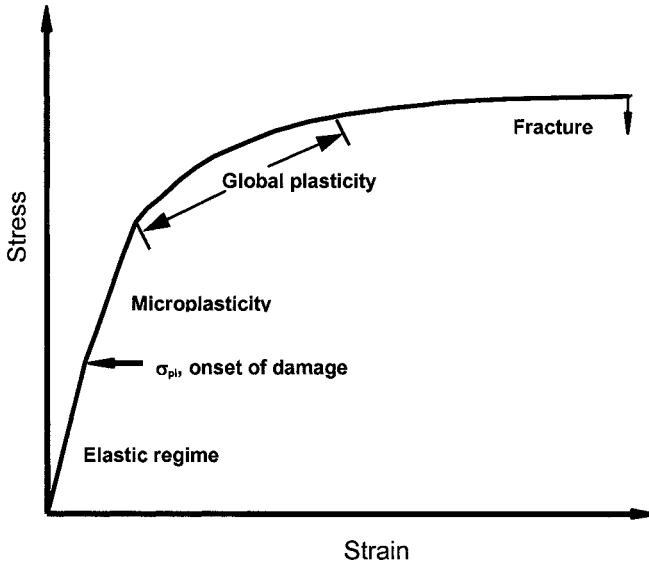
Fig. 7.1 Schematic of damage evolution in MMCs under tensile loading.

approaches its fracture stress, which results in particle fracture and fracture of the composite. It should be pointed out that the damage evolution will also be very much influenced by the strength and nature of the reinforcement/matrix interface, as discussed in sections 7.2 and 7.3 below.

7.1.1 Direct Strengthening

The strengthening mechanisms observed in MMCs may be divided into two broad categories, direct and indirect strengthening. Direct strengthening takes place primarily in continuous fiber reinforced composites, but also takes place in discontinuously reinforced composites. Under an applied load, the load is transferred from the weaker matrix, across the matrix/reinforcement interface, to the typically higher stiffness reinforcement (Cox, 1952; Kelly and Lilholt, 1969; Cheskis and Heckel, 1970; Kelly, 1973; Chawla, 1997; Chawla and Shen, 2001). In this manner, strengthening takes place by the reinforcement "carrying" much of the applied load. This is shown schematically in Fig. 7.2. Let's assume a single high stiffness fiber embedded in a lower modulus matrix. The composite is loaded without direct loading of the fiber itself. If a set of parallel imaginary lines are drawn on the composite, after loading the lines will become distorted because of the shear stresses generated by differing axial displacements in fiber and matrix. Thus, load transfer to the fiber occurs by means of shear strains in the matrix.

Let us consider the case of a purely elastic fiber in an elastic matrix mathematically, Fig. 7.3. Let u be displacement in the matrix in the presence of the fiber, at a distance x from one end, and let v be the displacement at x in the absence of the fiber. If P_f is the normal load on the fiber, then we can write the following expression for load transfer from the matrix to the fiber:

$$\frac{dP_f}{dx} = B(u - v) \tag{7.1}$$

where B is a constant that is a function of fiber arrangement and matrix and

(a)

(b)
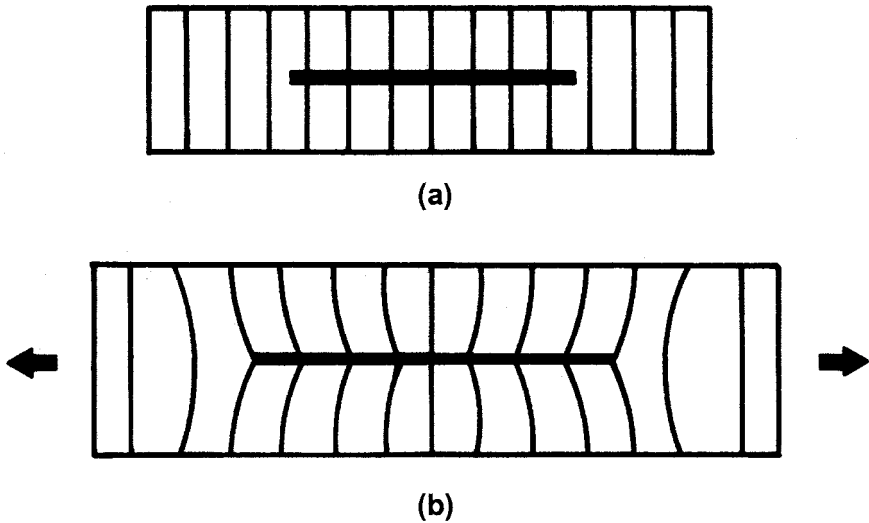
Fig. 7.2 A single fiber embedded in a matrix with lower modulus: (a) unstressed state and (b) stressed state. The imaginary vertical lines become distorted, indicating shear strains at the interface and load transfer to the fiber.
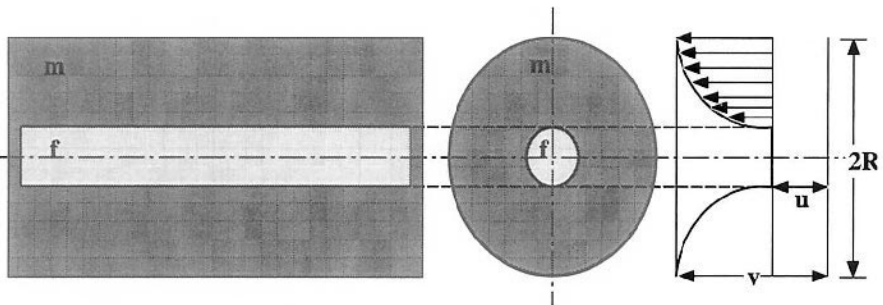
Fig. 7.3 A single fiber embedded in a cylindrical matrix shell subjected to an axial strain, e, which causes displacements in the fiber (u) and in the matrix (v).

fiber properties. The exact expression for B is described later in this section. Differentiating eq. 7.1, we get:

$$\frac{d^2 P_f}{dx^2} = B\left(\frac{du}{dx} - \frac{dv}{dx}\right) \tag{7.2}$$

where $\dfrac{du}{dx}$ is the strain in fiber $= \dfrac{p_f}{E_f A_f}$ and

$\dfrac{dv}{dx}$ is the strain in the matrix away from the fiber = e, imposed strain

Equation 7.2 can be rewritten as:

$$\frac{d^2 P_f}{dx^2} = B\left[\frac{P_f}{A_f E_f} - e\right]$$

This second-order differential equation has the following solution:

$$P_f = E_f A_f e + S \sinh \beta x + T \cosh \beta x$$

where $\beta = \sqrt{\dfrac{B}{A_f E_f}}$.

In order to evaluate the integration constants, S and T, we apply the boundary conditions, $P_f = 0$ at $x = 0$ and $x = \ell$. Using half-angle trigonometric relations we obtain the following result:

$$P_f = E_f A_f e \left[1 - \frac{\cosh \beta \left(\dfrac{\ell}{2} - x\right)}{\cosh \dfrac{\beta \ell}{2}}\right] \quad \text{for } 0 < x < \ell/2 \tag{7.3a}$$

or

$$\sigma_f = \frac{P_f}{A_f} = \frac{E_f e}{\ell} \left[1 - \frac{\cosh\beta\left(\dfrac{\ell}{2} - x\right)}{\cosh\dfrac{\beta\ell}{2}} \right] \quad \text{for } 0 < x < \ell/2 \quad (7.3b)$$

The maximum possible value of strain in the fiber is the imposed strain, e, so the maximum stress in the fiber is eE_f. The parameter β is a measure of how fast the load is transferred from the matrix to the fiber from the two ends. A value of $\beta = 0.5$ indicates a linear dependence of load transfer. If we have a long enough fiber, Fig. 7.4, the stress in the fiber will increase from both ends to a maximum value of the ultimate tensile strength of the fiber, i.e., $\sigma_{fu} = E_f e$. Only a portion of the fiber (in the center) will be under the maximum stress. The *average* stress in the fiber, then, can be written as:

$$\bar{\sigma}_f = \frac{E_f e}{\ell} \int_0^\ell \left[1 - \frac{\cosh\beta\left(\dfrac{\ell}{2} - x\right)}{\cosh\dfrac{\beta\ell}{2}} \right] dx = E_f e \left[1 - \frac{\tanh\dfrac{\beta\ell}{2}}{\dfrac{\beta\ell}{2}} \right]$$

We can obtain the variation of shear stress, τ, along the fiber/matrix interface by considering the equilibrium of forces acting over an element of fiber (radius r_f). Thus, we can write, from Fig. 7.4:

$$\frac{dP_f}{dx} dx = 2\pi r_f dx \tau \qquad (7.4)$$

Let us now consider the variation of shear stress, τ, along the fiber/matrix interface. We can obtain an expression for the interfacial shear stress by considering the equilibrium of forces over an element of fiber. The tensile load on the fiber, P_f, is equal to $P_f = \sigma_f \pi r_f^2$. Substituting this into eq. 7.4 we get:

$$\tau = \frac{1}{2\pi r_f} \frac{dP_f}{d\ell} = \frac{r_f}{2} \frac{d\sigma_f}{dx} \qquad (7.5)$$
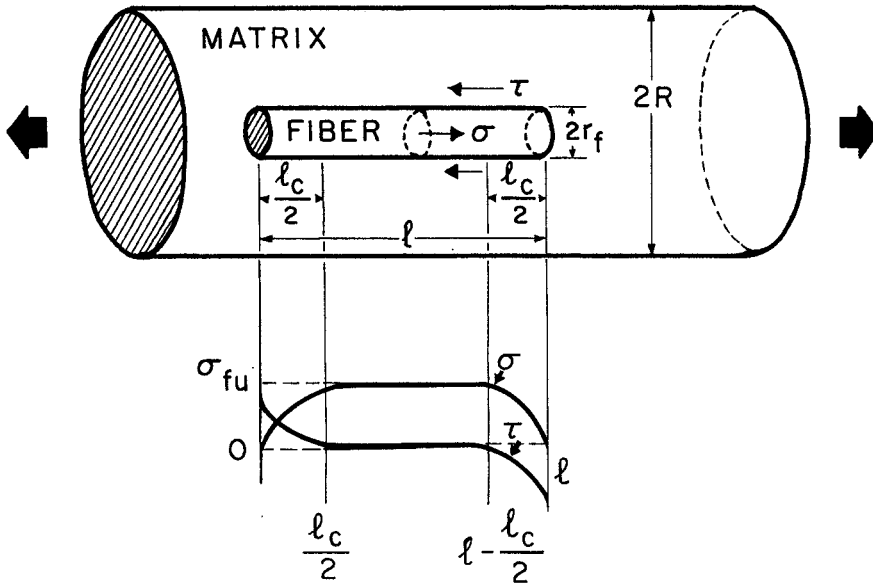
From eqs. 7.3(b) and 7.5 we obtain:

Fig. 7.4 Tensile stress (σ) and shear stress (τ) distribution in a single fiber embedded in a cylindrical matrix shell.

$$\tau = \frac{E_f r_f e \beta}{2} \frac{\sinh \beta (\ell/2 - x)}{\cosh \beta \ell/2}$$

Figure 7.4 shows the variation of τ and σ with distance x. At the ends of the fiber, the axial stress is zero. It increases until it reaches σ_{fu} in the center of the fiber (assuming a sufficiently long fiber that will enable the stress to build to σ_{fu}). The shear stress is a maximum at the fiber ends, and a minimum in the center of the fiber. Such a stress distribution has also been confirmed by finite difference technique (Termonia, 1987) and by micro-Raman spectroscopy for polymer matrix composites (Young, 1994).

We now return to the expression for the constant B, which is a function of fiber packing geometry. In Fig. 7.4 we note that 2R is the average center-to-center fiber spacing. Let $\tau(r)$ represent the shear stress at a distance r from the fiber axis. Then at the fiber surface we can be written as:

$$\frac{dP_f}{dx} = -2\pi r_f \tau(r_f) = B(u - v)$$

Or

$$B = -\frac{2\pi r_f \tau(r_f)}{(u - v)} \tag{7.6}$$

Consider now the equilibrium of forces on volume of matrix material between r_f and R. We can write:

$$2\pi r \tau(r) = \text{constant} = 2\pi r_f \tau(r_f)$$

$$\tau(r) = \frac{r_f \tau(r_f)}{r}$$

The shear strain in the matrix at a distance r is given by:

$$\tau(r) = G_m \gamma$$

where G_m is the shear modulus of the matrix and γ is the shear strain in the matrix. The shear strain in the matrix is given by

$$\gamma = \frac{dw}{dr} = \frac{\tau(r)}{G_m} = \frac{\tau(r_f)r_f}{G_m r}$$

where w is the real displacement in the matrix at any distance r. Integrating the above expression between the surface of the fiber, r_f and the outer radius of the matrix, R, gives us the total displacement in the matrix:

$$\int_0^R dw = \Delta w = \frac{\tau(r_f)r_f}{G_m} \int_0^R \frac{1}{r} dr = \frac{\tau(r_f)r_f}{G_m} \ell n\left(\frac{R}{r_f}\right) \tag{7.7}$$

We can also write for the total displacement as:

$$\Delta w = v - u = -(u - v) \tag{7.8}$$

From Eqs. (7.7) and (7.8), we obtain the following relationship:

$$\frac{\tau(r_f)r_f}{u-v} = -\frac{G_m}{\ln(R/r_f)}$$ (7.9)

From Eqs. (7.6) and (7.9), we get:

$$B = \frac{2\pi G_m}{\ln(R/r_f)}$$ (7.10)

B is related to load transfer parameter β as follows:

$$\beta = \left(\frac{B}{E_f A_f}\right)^{\frac{1}{2}} = \left[\frac{2\pi G_m}{E_f A_f \ln(R/r_f)}\right]^{\frac{1}{2}}$$ (7.11)

The ratio R/r_f is a function fiber packing. For a square array and hexagonal array of fibers, we can write the following two expressions:

$$\ln\left(\frac{R}{r_f}\right) = \frac{1}{2}\ln\left(\frac{\pi}{V_f}\right) \quad \text{(square array)}$$

$$\ln\left(\frac{R}{r_f}\right) = \frac{1}{2}\ln\left(\frac{2\pi}{\sqrt{3}V_f}\right) \quad \text{(hexagonal array)}$$

A more general, maximum fiber packing factor, ϕ_{max}, can also be introduced into the above equation:

$$\ln\left(\frac{R}{r_f}\right) = \frac{1}{2}\ln\left(\frac{\phi_{max}}{V_f}\right)$$

Substituting into Eq. (7.11), we get:

$$\beta = \left[\frac{4\pi G_m}{E_f A_f \ln(\phi_{max}/V_f)}\right]^{\frac{1}{2}}$$

From the discussion above, it can be seen that in order to load the fibers to their ultimate tensile strength, the matrix shear strength must be relatively high. The maximum shear stress will be the smaller of the following two stresses: (a) yield stress of the matrix in shear and (b) shear strength of the fiber/matrix interface. In MMCs, the interface shear strength is quite high, so plastic yielding of the matrix will take place first. If we assume that the matrix does not work-harden, the matrix shear yield strength, τ_y will control the load transfer. Then, the equilibrium of forces over a fiber length $\ell/2$ (since the fiber is loaded from both ends) gives us the following relation:

$$\sigma_f \frac{\pi d^2}{4} \ell = \tau_y \pi d \frac{\ell}{2} \quad \text{or} \quad \frac{\ell}{d} = \frac{\sigma_f}{2\tau_y} \qquad (7.12)$$

The term ℓ/d is called the aspect ratio of the fiber. Given a sufficiently long fiber, it should be possible to load the fiber to its ultimate tensile strength, σ_{fu}, by means of load transfer through the plastically deforming matrix. Thus, in order to load the fiber to σ_{fu}, a critical aspect ratio of fiber is required, $(\ell/d)_c$, which is obtained by rewriting Eq. (7.12):

$$\left(\frac{\ell}{d}\right)_c = \frac{\sigma_{fu}}{2\tau_y} \qquad (7.13)$$

Thus, in order to load the fiber to σ_{fu} at a single point, ℓ must be equal to ℓ_c. In order to load a larger fraction of the fiber to σ_{fu}, ℓ should be much larger than ℓ_c. Thus, load transfer is more efficient in composites with large aspect ratio reinforcement, such as continuous fibers or whiskers. Due to the lower aspect ratio of particulate materials, load transfer is not as efficient as in the case of continuous fiber reinforcement, but is still significant in providing strengthening (Nardone and Prewo, 1986; Davis and Allison, 1993; Chawla et al., 1998a; Chawla et al. 2000).

Nardone and Prewo (1986) proposed a modified shear lag model for load transfer in particulate materials, Fig. 7.5. The model incorporates load transfer from the particle ends, which is neglected in fiber reinforced composites because of the large aspect ratio. The yield strength of the particulate composite, σ_{cy}, is increased over the matrix yield strength, σ_{my}:

$$\sigma_{cy} = \sigma_{my}\left[V_p\left(\frac{S+4}{4}\right) + V_m\right]$$
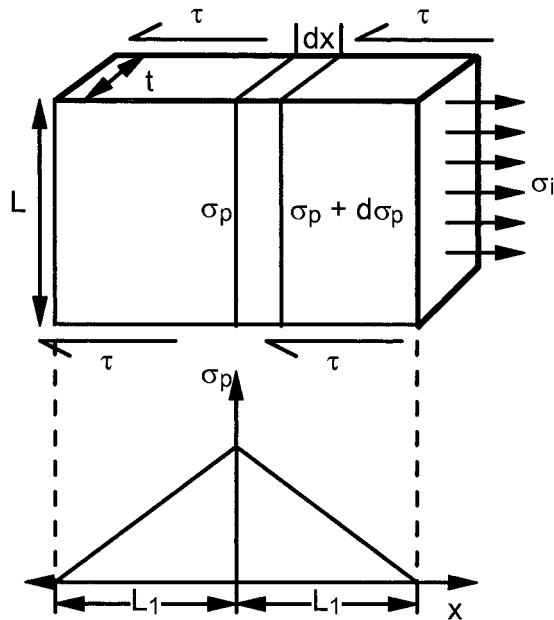
Fig. 7.5 Schematic of modified shear lag analysis used to quantify load transfer in low aspect ratio particles (after Nardone and Prewo, 1986).

where S is the aspect ratio of the particle (equal to the particle length, L, divided by the particle thickness, t, for a rectangular particle), V_p is the volume fraction of particles, and V_m is the volume fraction of matrix. Note that this relation does not account for particle size or matrix microstructure effects on load transfer.

7.1.2 Indirect Strengthening

Indirect strengthening arises from a change in matrix microstructure and properties due to the addition of reinforcement. In this section we describe some possible sources of indirect strengthening. Thermal expansion mismatch between reinforcement and matrix can result in internal stresses whenever there is a temperature change (e.g., during cool down from processing or during service). Such a mismatch is generally present in all kinds of composites. It is a very important feature of MMCs comprised as they are of a high coefficient of thermal expansion (CTE) metallic matrix and a low CTE ceramic reinforcement. If the thermal mismatch-induced stress is greater than the yield stress of the matrix, upon cooling, dislocations form at the reinforcement/matrix interface because plastic deformation in common metals occurs via dislocations. In this manner, thermally-induced dislocation punching results in "indirect strengthening" of the matrix

(Chawla and Metzger, 1972; Chawla, 1973a; Chawla, 1973b; Vogelsang et al., 1986; Arsenault and Shi, 1986; Dunand and Mortensen, 1991). Chawla and Metzger (1972) showed this effect in W fiber reinforced Cu single crystal matrix composites. The density of dislocations in the matrix was measured (by an etch pitting technique) as a function of distance from the fiber/matrix interface, for composites with various volume fractions of W fiber, Fig. 7.6(a). With increasing volume fraction, the dislocation density in the matrix increased. The dislocation density was also highest in the interface region because the thermal stresses between fiber and matrix in the interface region are the highest. The three-dimensional thermal stress model described in chapter 6 can be used to explain the distribution of dislocation density in the matrix. Fig. 7.6(b) shows thermally-induced slip lines in the polycrystalline Cu matrix in a W/Cu composite that was thermally cycled between room temperature and 450°C. Dunand and Mortensen (1991) used a model system of glass fiber reinforced AgCl to study dislocation punching due to thermal mismatch. The AgCl matrix is optically transparent and the dislocations can be seen emanating from the fiber, Fig. 7.7. The degree of thermally-induced dislocations can also be exacerbated by the degree of fiber roughness (Isaacs and Mortensen, 1992).

Arsenault and Shi (1986) developed a model to quantify the degree of dislocation punching that takes place due to CTE mismatch between a particle and matrix, Fig. 7.8. The dislocation density generated due to the mismatch is given by:

$$\rho_{CTE} = \frac{A\varepsilon V_p}{b(1 - V_p)d} \qquad (7.14)$$

where A is a geometric constant, b is the Burgers vector, d is the diameter of the particle, V_p is the particle volume fraction, and ε is the thermal misfit strain equal to $\Delta\alpha\Delta T$. The incremental increase in strength due to dislocation punching, then, can be written as:

$$\Delta\sigma = BGb\rho_{CTE}^{1/2}$$

where B is a constant and G is the shear modulus of the matrix. Substituting in Eq. 7.14, we can write $\Delta\sigma$ as:

$$\Delta\sigma = BGb\left[\frac{A\varepsilon V_p}{b(1 - V_p)}\frac{S}{d}\right]^{\frac{1}{2}} \qquad (7.15)$$
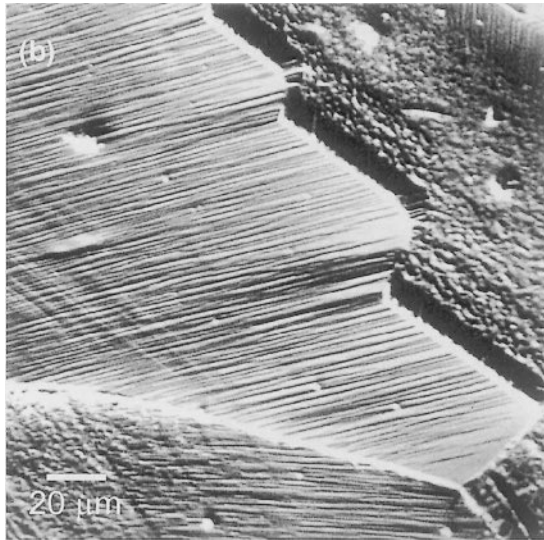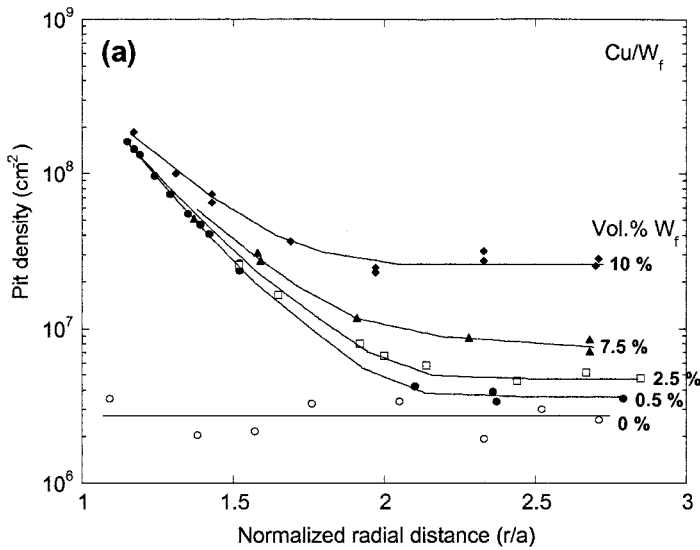
Fig. 7.6 (a) Dislocation density in W fiber reinforced Cu matrix composites, as a function of distance from the fiber/matrix interface. With increasing volume fraction of fiber, the thermal stress mismatch at the interface increased, resulting in a higher dislocation density (after Chawla and Metzger, 1972). (b) Thermally-induced slip lines in the Cu matrix.
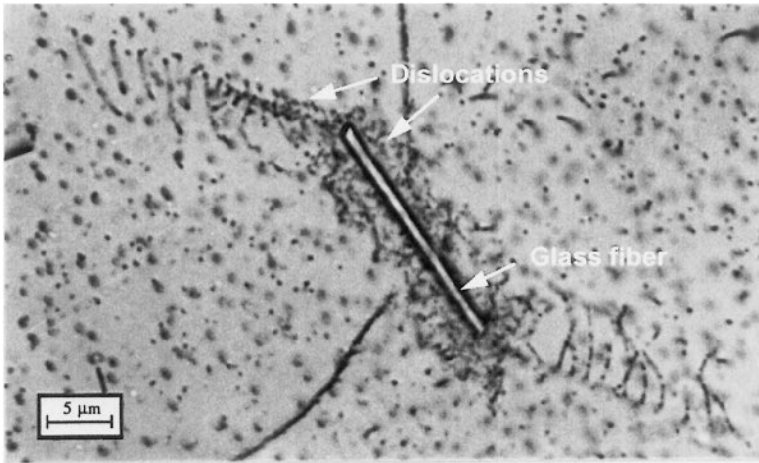
Fig. 7.7 Thermally-induced dislocation punching in a model glass fiber/AgCl system (Dunand and Mortensen, 1991). Note the high density of dislocations at the interface, and the punching of dislocation loops from the fiber ends (courtesy of A. Mortensen and reprinted with permission of Elsevier Ltd.).
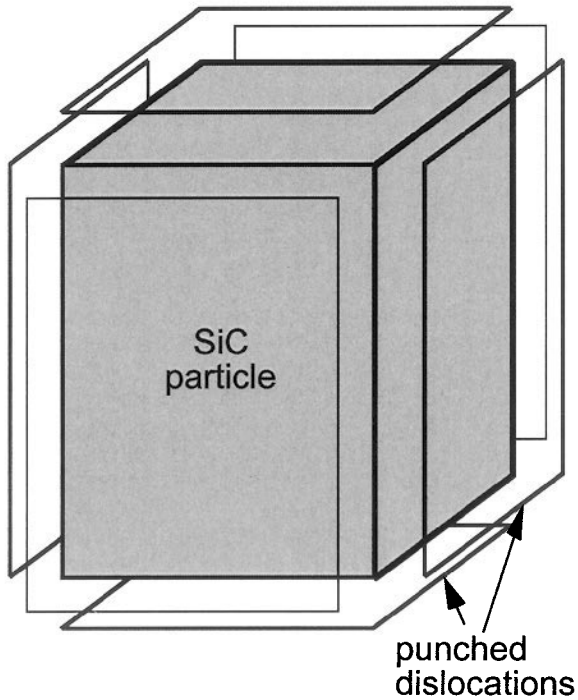

Fig. 7.8 Schematic of model used to quantify the degree of dislocation punching that takes place due to CTE mismatch between particle and matrix (after Arsenault and Shi, 1986).

where S is the aspect ratio of the particle and the other symbols have the significance given above. Inspection of Eq. 7.15 shows that the degree of indirect strengthening is directly proportional to volume fraction and inversely proportional to particle size. Thus, a larger degree of interfacial area (i.e., smaller particle size) will result in enhanced dislocation punching. This is shown schematically in Fig. 7.9. Note that for a constant volume fraction of 0.3, a significant enhancement in indirect strengthening is observed for particles of 3 μm diameter, vis-à-vis particles of 100 μm diameter

In age-hardenable matrix materials, the thermally-induced dislocations (formed upon quenching from the solution treatment) serve as heterogeneous nucleation sites for precipitate formation during the aging treatment (Suresh and Chawla, 1993). Not only is there a preferential distribution of precipitates in the particle/matrix interface region, but the higher density of dislocations also causes an acceleration in the time to peak-age compared to the unreinforced alloy of the same composition.

In composites processed by liquid phase routes, the matrix grain size can be much finer than that of the unreinforced alloy, due to pinning of grain boundaries by the particles or Zener pinning (Humphreys, 1977;
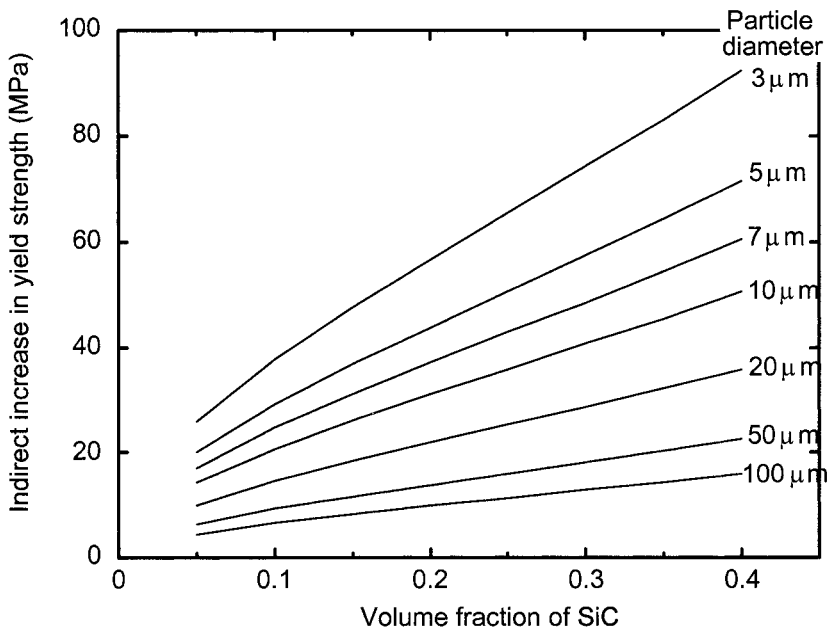
Fig. 7.9 Increase in yield strength due to dislocation punching, as predicted by the model of Arsenault and Shi (1986). The degree of strengthening is significantly influenced by particle size, for a given volume fraction.

Humphreys, 1991). Differences in matrix texture may also result by the incorporation of reinforcement, for example, in deformation processed materials (see chapter 4).

Separating and quantifying the contributions of direct and indirect strengthening, to the overall composite strength is a challenge. The extent of indirect strengthening is more difficult to quantify than the contribution from direct strengthening. One way to separate the two types of strengthening is to process composites such that the matrix microstructure is similar to that of the unreinforced alloy. Krajewski et al. (1993), used a thermomechanical treatment in Al 2080/SiC$_p$, consisting of solution treating, rolling, followed by aging (T8 treatment) to provide a homogeneous distribution of dislocations (and subsequently precipitates) in both the matrix of the composite and the unreinforced alloy. In such a situation, the difference in strengthening between unreinforced alloy and composite was attributed primarily to load transfer to the reinforcement (Chawla et al., 1998a). This is shown in Fig. 7.10. Chawla et al., (1998a) showed that in T8 matrix
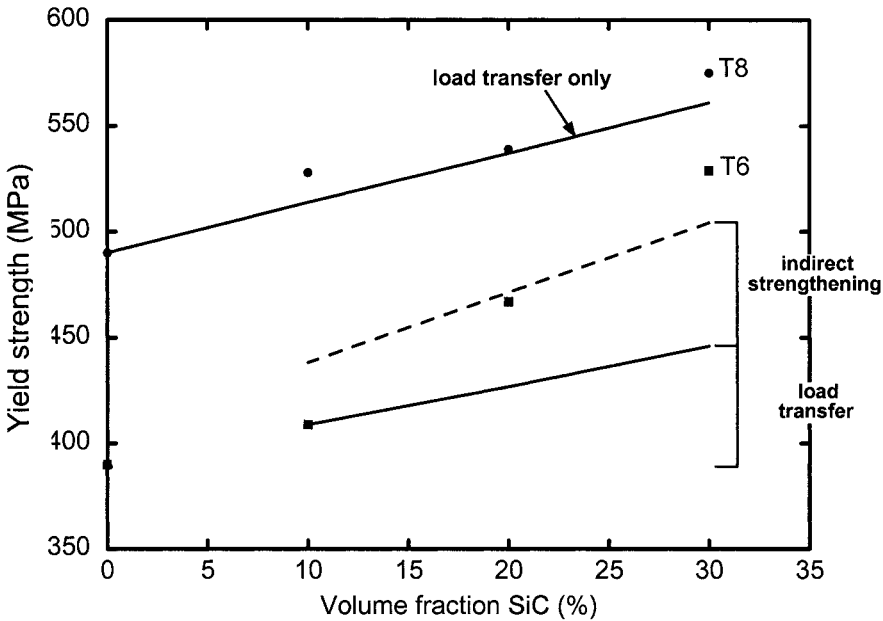
Fig. 7.10 Yield strength vs. volume fraction of SiC particles in 2080/SiC$_p$ composite (after Chawla et al., 1998a). The rolled and aged materials (T8 matrix composites) have similar microstructure to the unreinforced T8 alloy. T6 matrix composites are aged only, so their microstructure is different from 2080-T6. The experimental increase in yield strength in T8 materials correlated well with predictions from the modified shear lag model. In T6 matrix composites, the strength of the composite consisted of contributions of both indirect and direct strengthening.

composites, the experimental increase in yield strength correlated well with predictions from the modified shear lag model. In composites that were solution treated, quenched, and aged (T6 heat treatment), the strength of the composite consisted of contributions of both indirect and direct strengthening, Fig. 7.10.

7.2   MONOTONIC   BEHAVIOR   OF   CONTINUOUS   FIBER REINFORCED MMCS

The monotonic strength and damage evolution in continuous fiber reinforced MMCs are dependent on several factors:

1. *Fiber characteristics.* The volume fraction, strength, and relative orientation of the fibers, with respect to the loading axis.

2. *Strength and nature of the interface.* Interfacial strength has a significant effect on the strengthening and damage tolerance of continuous fiber reinforced MMCs. Interfacial reactions between fiber and matrix, and fiber dissolution, may be detrimental to the strength of the composite. Preferential precipitation at the interface, in age-hardenable systems, can have mixed effects on strength.

3. *Matrix work hardening and strength characteristics.* Of particular importance are the changes in matrix microstructure, during processing, due to the incorporation of the reinforcement (i.e., indirect strengthening, described above).

We now examine each of the three main factors described above. Continuous fiber reinforced MMCs exhibit very high strength in the direction parallel to the fibers, but comparatively low strength perpendicular to the fiber direction. Figure 7.11 shows the anisotropy in strength of Al-2.5Li/$Al_2O_{3,f}$ composites, parallel to the fibers ($0°$) and perpendicular to the fiber direction ($90°$), in both tension and compression (Schulte and Minoshima, 1993). Clearly, along the axis of the fibers the degree of strengthening from the fibers will be much higher than that perpendicular to the fiber direction. The mechanical properties of fiber reinforced metal matrix composites are also very much dependent on the strength of the fiber/matrix interface. Figure 7.12 shows a schematic of damage for the case of a relatively weak fiber/matrix interface and that of a relatively strong interface. When a fiber fractures in the composite with a weak interface, fiber debonding and crack deflection take place. These local energy-absorbing mechanisms allow for uniform redistribution of the load, originally borne by the fractured fiber, to the surrounding fibers. This
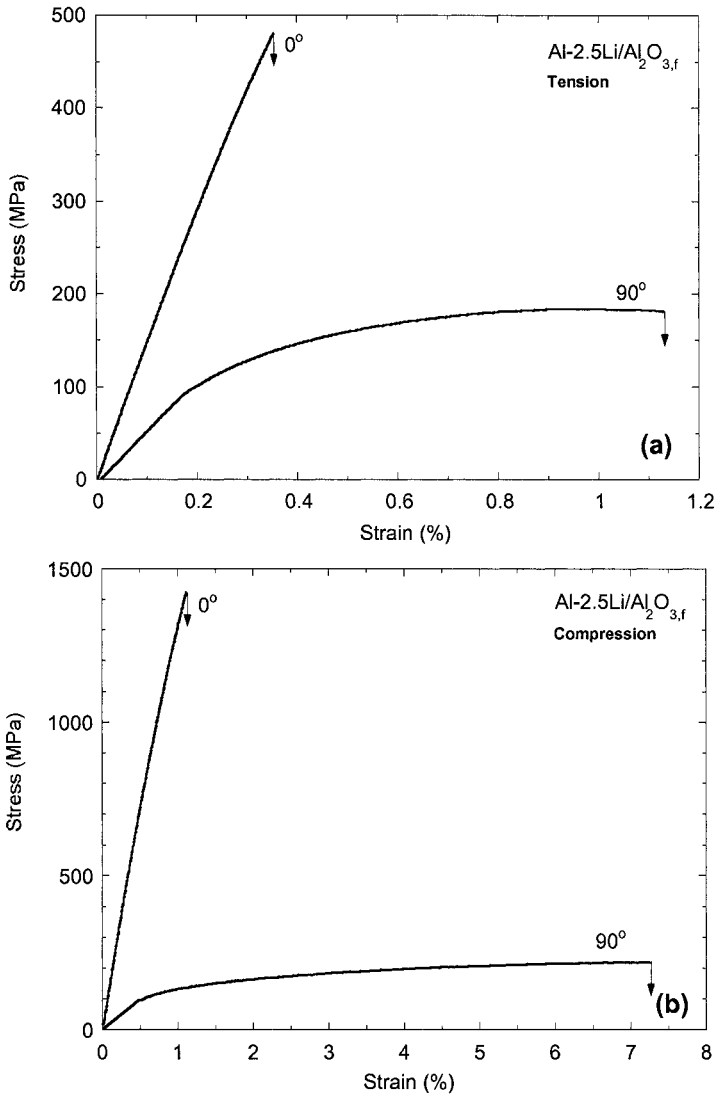
Fig. 7.11 Anisotropy in strength of $Al-2.5Li/Al_2O_{3,f}$ composites, parallel to the fibers ($0°$) and perpendicular to the fiber direction ($90°$), in (a) tension and (b) compression (after Schulte and Minoshima, 1993).
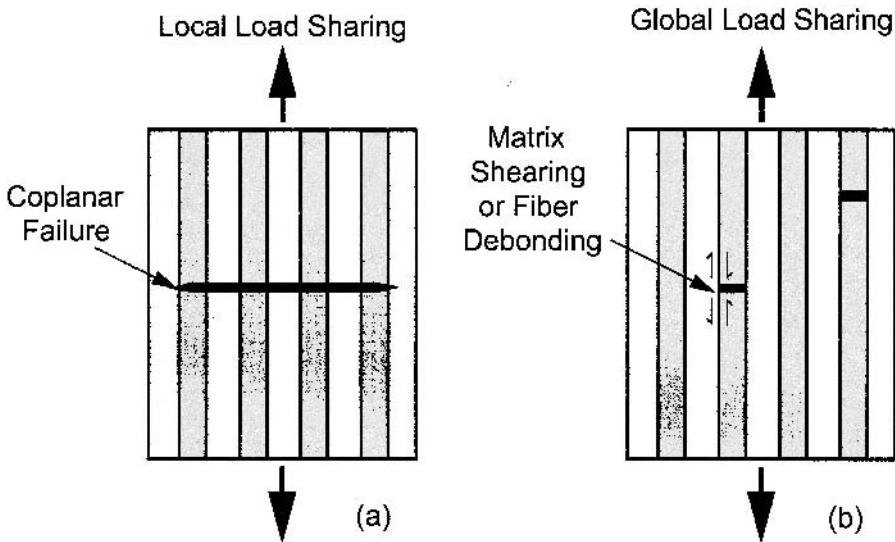
Fig. 7.12 Schematic of damage for the case of: (a) relatively strong fiber/matrix interface, resulting in local load sharing and coplanar failure, and (b) relatively weak interface, where global load sharing is observed, and fiber debonding and matrix shear are predominant.

condition is called *global load sharing* (Curtin, 1993). When the interface strength is very large, fiber fracture will not result in debonding and crack deflection. Rather, the load cannot be redistributed homogeneously, so the single fiber fracture will result in precipitous fracture of adjacent fibers. As the neighboring fibers fracture, more and more fibers will continue to fracture until the composite fails. This series of successive fiber failures due to localization of strain around a single fiber results in *local load sharing* (Gonzalez and LLorca, 2001). It should be noted that a very weak interface is also not desirable in MMCs. Such an interface would not allow efficient load transfer from the matrix to the fiber.

Whether a composite exhibits global or local load sharing behavior may also be influenced by the work hardening characteristics of the matrix. A matrix with high strain hardening rate would be less conducive to plastic relaxation of the stress concentration around the fractured fiber. Thus, more brittle matrix materials are more conducive to local load sharing and a lower ductility. Figure 7.13 shows a comparison of $Al/Al_2O_3/60_f$ and $6061/Al_2O_3/60_f$ fiber reinforced composites (Devé and McCullough, 1995).
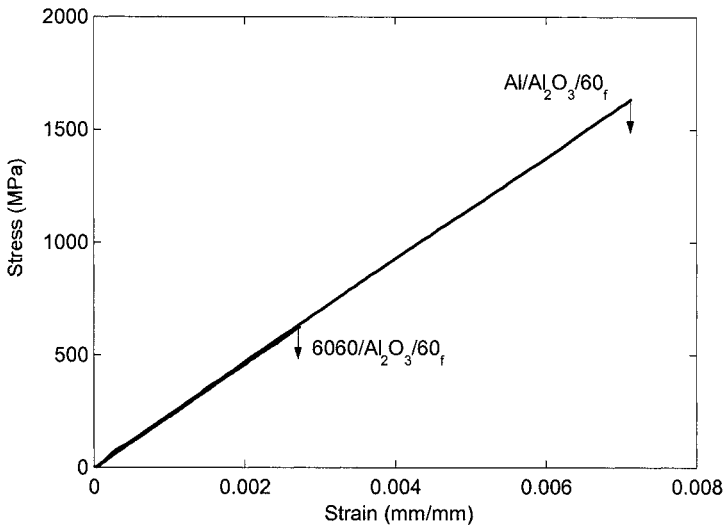
Fig. 7.13 Tensile stress-strain comparison of Al/Al$_2$O$_3$/60$_f$ and Al6061/Al$_2$O$_3$/60$_f$ fiber reinforced composites (after Devé and McCullough, 1995). The high interfacial shear strength and higher matrix work hardening rate of the Al6061 matrix, resulted in a much lower ductility and strength than the composite with pure Al matrix.

Because of the combined effects of high interfacial shear strength and higher matrix work hardening rate of the Al 6061 matrix, this composite has a much lower ductility and strength than the composite with the pure Al matrix. Voleti et al. (1998) used a finite element model of a composite consisting of a broken fiber surrounded by the matrix and an intact fiber. They showed that the stress concentration in the intact fiber was influenced by both interfacial debonding and matrix plasticity surrounding the broken fiber. If fiber fracture takes place at very low strains (much below the onset of global plasticity), then the matrix plasticity "propagates" toward the intact fiber resulting in a large degree of stress elevation. Interfacial debonding, on the other hand, reduces the stress concentration around the fractured fiber and the intact fiber.

The degree of global load sharing is also a function of strain rate. Galvez et al. (2001) tested large diameter SiC fiber reinforced Ti-6Al-4V matrix composites at strain rates ranging between 2×10^{-5} and 500 s^{-1}. It was shown that at very high strain rates local load sharing conditions were predominant, and a lower composite ductility was observed. Lower strain rates were more conducive to allowing a gradual redistribution of the load, so global load sharing was observed. Microstructural observations showed that at low strain rates the carbon coating on the SiC fiber resulted in crack deflection at the

interface, while at very high strain rates the cracks penetrated the coating. These authors did not, however, observe a strain rate dependence on strength of the composite.

Guden and Hall (2000) noticed significant increases in compressive flow stress and strength with increasing strain rate in $Al/Al_2O_{3,f}$ composites. The strain rate sensitivity was observed in both longitudinal and transverse orientations. The strain rate sensitivity of transverse strength was attributed to the matrix strain rate sensitivity, while that in the longitudinal direction was due to strain rate dependent fiber buckling. In static compression, significant kinking and buckling of the fibers also takes place (Deve, 1997). Unfortunately, while relatively weak interfaces are conducive to global load sharing and thus, high tensile strength and ductility, they are quite detrimental to the transverse properties of the composite (Jansson et al., 1991; McCullough et al., 1994; Bushby, 1998). This can be explained by the fact that, under transverse loading, the weak interfaces are perpendicular to the applied load. Similar observations have been made for Al_2O_3 fiber/Mg matrix composites under off-axis loading (Hack et al., 1984).

7.2.1 Criteria for Debonding and Crack Deflection at an Interface

In MMCs, as well as in other types of composites, interfacial bonding affects the fracture behavior of the composite. In very general terms, a strong interfacial bond will allow an oncoming crack to go unimpeded through the interface and the composite will fail, more or less, in one plane and in a brittle manner. The interaction of a crack with a weak interface, on the other hand, is likely to lead to debonding at the interface, followed by crack deflection, crack bridging, fiber fracture, and finally fiber pullout. These are all energy absorbing phenomena that contribute to enhanced fracture toughness and a non-catastrophic failure mode.

A strength-based model for crack deflection or the formation of secondary crack at a weak interface was first proposed by Cook and Gordon (1964). They analyzed the problem of crack deflection at an interface between materials of identical elastic constants, i.e., the same material joined at an interface. Consider a crack advancing perpendicular to the fiber/matrix interface. Cook and Gordon (1964) estimated the strength of the interface necessary to cause a diversion of the crack from its original direction. At the tip of a crack, there exists a triaxial state of stress (plane strain) or a biaxial stress (plane stress), see Fig. 7.14. The principal stress component, σ_y, has a very high value at the crack tip, and decreases sharply with distance from the crack tip. The stress component acting normal to the interface, σ_x, is zero at the crack tip. It rises to a maximum value at a small distance from the crack

tip and then falls off in a manner similar to σ_y. If the tensile strength of the interface is less than the maximum value of σ_x, then the interface will fail in front of the crack tip. According to the estimates of Cook and Gordon, an interface with strength equal to or less than $1/5^{th}$ of σ_x will result in the opening of the interface in front of the crack tip.

One can also analyze the interaction between a crack and an interface in terms of a fracture energy parameter instead of strength (He and Hutchinson, 1989). Two materials meeting at an interface are more than likely to have *different* elastic constants. The modulus mismatch leads to shearing of the crack surfaces. This results in a mixed-mode stress state in the vicinity of an interface crack tip involving both the tensile and shear components. This, in turn, results in mixed-mode fracture, which can occur at the crack tip or in the wake of the crack. Figure 7.15 shows this crack front and crack wake debonding in a fiber reinforced composite. What this means in practical terms is that instead of a simple, one parameter description by the critical stress intensity factor K_{Ic}, one needs a more complex formalism of fracture mechanics to describe the situation in the composite. The parameter K under such a situation becomes scale sensitive, but the critical strain energy release rate, G_{Ic}, is not a scale sensitive parameter. The strain energy release rate, G is a function of the phase angle, ψ, which is a function of normal and shear loading.

One needs to specify G and ψ to analyze the debonding at the interface. G and ψ are related, through the so-called Dundurs parameters, α and β as defined below:
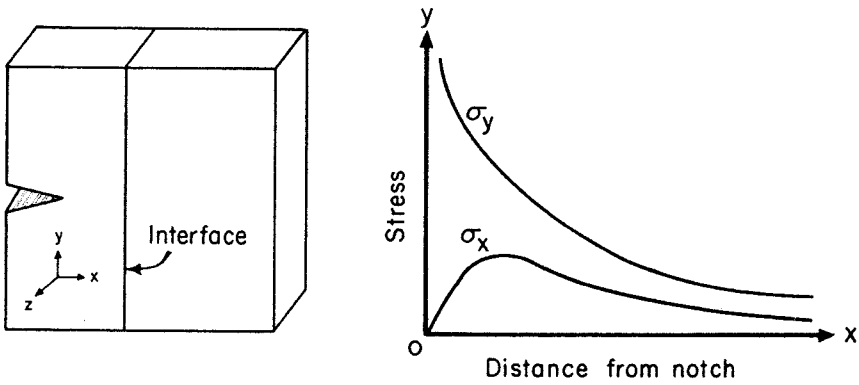
$$\alpha = \frac{G_1(1-v_2)-G_2(1-v_1)}{G_1(1-v_2)+G_2(1-v_1)}$$

$$\beta = \frac{1}{2}\frac{G_1(1-2v_2)-G_2(1-2v_1)}{G_1(1-v_2)+G_2(1-v_1)}$$

The parameter α can also be defined as:

$$\alpha = \frac{\overline{E}_1 - \overline{E}_2}{\overline{E}_1 + \overline{E}_2}$$

$$\overline{E} = \frac{E}{1-v^2}$$

Fig. 7.14 Stress distribution at a crack tip under a uniaxial applied stress in the y-direction (after Cook and Gordon, 1964). σ_y has a very high value at the crack tip, and decreases sharply with distance from the crack tip. The stress component acting normal to the interface, σ_x, is zero at the crack tip; it rises to a maximum value at a small distance from the crack tip and then falls off in a manner similar to σ_y.
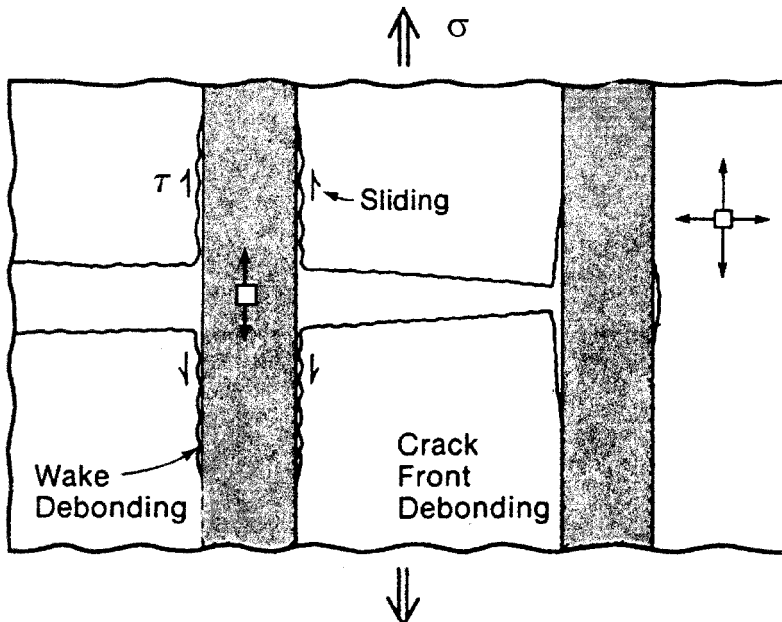
Fig. 7.15 Crack front and crack wake debonding in a fiber reinforced composite under a far field, uniaxial stress, σ. Note the interfacial shear stress, τ causing sliding and triaxial state of stress at the crack tip.

In the above expressions, ν is the Poisson's ratio, E is Young's modulus, and the subscripts 1 and 2 refer to the interface and fiber, respectively. The expression for the phase angle, ψ, in terms of the elastic coefficients of the two media, radius r from the crack tip, and the displacements, u and v, at the crack tip is as follows:

$$\phi = \tan^{-1}\left(\frac{v}{u}\right)$$

$$\psi = \phi - \left(\frac{\ln r}{2\pi}\right)\ln\frac{(1-\beta)}{(1+\beta)}$$

These expressions have been used by several researchers (Ruhle and Evans, 1988; He and Hutchinson, 1989; Evans and Marshall, 1989; Gupta et al., 1993; Chan, 1993) to analyze the conditions for fiber/matrix debonding in terms of the energy requirements. Without going into the details of the model, the main message of such a plot is to display the conditions under which the crack will deflect along the interface or penetrate through the interface into the fiber. The chart of G_i/G_f vs. α is shown in Fig. 7.16. G_i is the mixed- mode interfacial fracture energy of the interface, G_f is the mode I fracture energy of the fiber, and α is a measure of elastic anisotropy as defined above. For opening mode or mode I, $\psi = 0°$ while for mode II, $\psi = 90°$. For all values of G_i/G_f below the line, interfacial debonding is predicted. For the special condition of $\alpha = 0$, i.e., zero elastic mismatch, the model
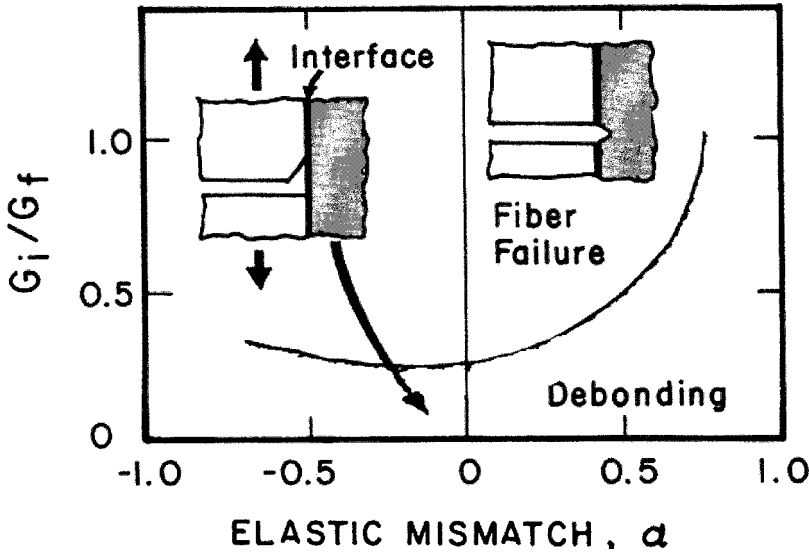

Fig. 7.16 A chart of relative energies, G_i/G_f vs. elastic mismatch, α (after Evans and Marshall, 1989).

predicts debonding at the fiber/matrix interface for G_i/G_f less than about 0.25. Conversely, for G_i/G_f greater than 0.25, the crack will propagate across the fiber. In general, for the elastic mismatch, α greater than zero, the minimum interfacial toughness required for interface debonding increases, i.e., high modulus fiber tends to favor debonding.

Gupta et al. (1993) have also derived strength and energy criteria for crack deflection at a fiber/matrix interface for several composite systems. They took due account of the anisotropic nature of the fiber as well as the fact that a crack can deflect along the interface in one direction (singly) or two directions (doubly). Their experimental technique involved laser spallation of a film from a substrate and the measurement of displacement by a sophisticated laser Doppler displacement interferometer. This technique allows the measurement of the tensile strength of the planar interface between the film and the substrate. The strength determined in the laser spallation experiment is thought to be independent of any inelastic processes because the interface separation takes place at a very high strain rate, about 10^6 s^{-1}. The tensile strength determined in this fashion is then related to the *intrinsic* interface toughness. According to the analysis of Gupta et al., for most pairs of materials, the energy release rate is higher for the doubly deflected crack than that for the singly deflected case. In this formulation, a generalized interface delamination chart based on the energy criterion cannot be made. However, the authors did provide the ratio of energies of crack deflection and crack penetration for a few chosen interface systems (Gupta, 1991; Gupta et al., 1993).

7.2.2 Work Done in Fiber Pullout

Fiber pullout can be an important feature of the failure process in fiber reinforced composites. We now derive an expression for the work done in the pullout process. Consider the situation depicted in Fig. 7.17. Let us say that the fiber, of diameter d, fractures at some distance k below the main crack plane, such that $0 < k < \ell_c/2$, where ℓ_c is the critical length for load transfer. Locally, debonding of the fiber/matrix interface occurs. When the fiber is pulled out of the matrix, an interfacial frictional shear stress, τ_i, will be generated. In our simple analysis here, we assume that this shear stress, τ_i, resisting fiber sliding is a constant. More complex treatments involving a Coulomb friction law governing fiber sliding resistance (Shetty, 1988; Gao et al., 1988) and treatments taking into account residual stresses are available in the literature (Cox, 1990; Hutchinson and Jensen, 1990; Kerans and Parthasarathy, 1991).
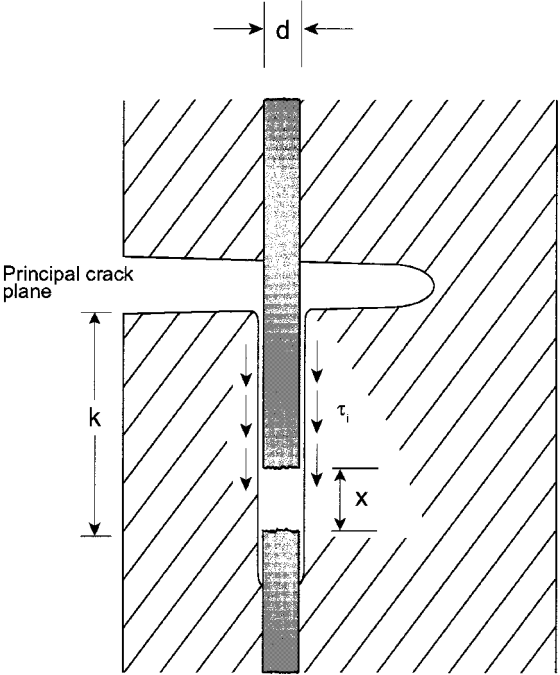
Fig. 7.17 Fiber pulled out through a distance x after fiber fracture. A shear stress, τ_i, comes into play at the interface during pullout.

Let the fiber be pulled out a distance x. The interfacial shear force opposing this motion of fiber is $\tau_i \pi d (k - x)$, where $\pi d (k - x)$ is the cylindrical surface area over which the shear stress is acting. Let the fiber be pulled out through a small distance dx. Then the work done by the interfacial shear force is $\tau_i \pi d (k - x)$ dx. The total work done in the fiber pullout process over the length k is obtained by integration:

$$\int_0^k \tau_i \pi d(k - x)\, dx = \frac{\tau_i \pi d k^2}{2}$$

The length of the fiber pulled out will vary between 0 and $\ell_c/2$, where ℓ_c is the critical length for load transfer. Therefore, the average work done in the fiber pullout process is:

$$W_{fp} = \frac{1}{\ell_c/2} \int_0^{\ell_c/2} \frac{\tau_i \pi d k^2\, dk}{2} = \frac{\tau_i \pi d \ell_c^2}{24}$$

This expression assumes that all of the broken fibers are pulled out. Experimental observations, however, show that only fibers with broken ends within a distance $\ell_c/2$ from the principal fracture plane undergo pullout. Thus, we should expect a fraction (ℓ_c/ℓ) of fibers to pullout, and the average work done per fiber in fiber pullout can be written as

$$W_{fp} = \frac{\ell_c}{\ell} \frac{\tau_i \pi d \ell_c^2}{24}$$

7.2.3 Effect of Interfacial Reactions on Monotonic Behavior

In chapter 4, we described the general features of the interface and provided some examples of interfacial reactions in MMCs. Here we explore the effects of interfacial reactions on the monotonic properties of MMCs. Interfacial reactions can play an important role in damage of continuous fiber reinforced MMCs (Page et al., 1984). In Ti matrix composites reinforced with SCS-6 fibers, the C-rich fiber coating reacts with the Ti matrix to form layers of brittle TiC and Ti_5Si_3 (Konitzer and Loretto, 1989; Leyens et al., 2003). In B fiber reinforced Al, AlB_2 is formed at the interface at temperatures as low as 500°C (Grimes et al., 1977). Tensile loading in the longitudinal axis results in circumferential cracks in the reaction layer, which severely impair the strength of the composite (Grimes et al., 1977; Mikata and Taya, 1985; Kyono et al., 1986). Figure 7.18(a) shows that the longitudinal strength decreases with increasing exposure time at 500°C (Kyono et al., 1986). In the transverse orientation, however, Figure 7.18(b), there was a slight increase in strength. This is because the damage mechanisms in transversely loaded composites were quite different. Here, the fracture surfaces of as-fabricated samples showed significant interfacial debonding. With increasing exposure time and an increase in the reaction layer thickness, the interface strength increased, so microcracks formed in the reaction layer and propagated through the boron fiber, resulting in fiber splitting.

Transverse strength may also be affected by binders used to densify the matrix of the composite. Eldridge et al. (1997) fabricated sapphire fiber reinforced NiAl matrix composites with and without a polymethyl methacrylate (PMMA) organic binder. Transverse fracture surfaces showed that the composites with the binder exhibited a large amount of carbon residue at the fiber/matrix interface, which prevented a strong interfacial mechanical bond and led to low interfacial strength, Fig. 7.19(a). Composites processed without binder had a much "cleaner" fracture surface, Figure 7.19(b), and stronger bond strength.
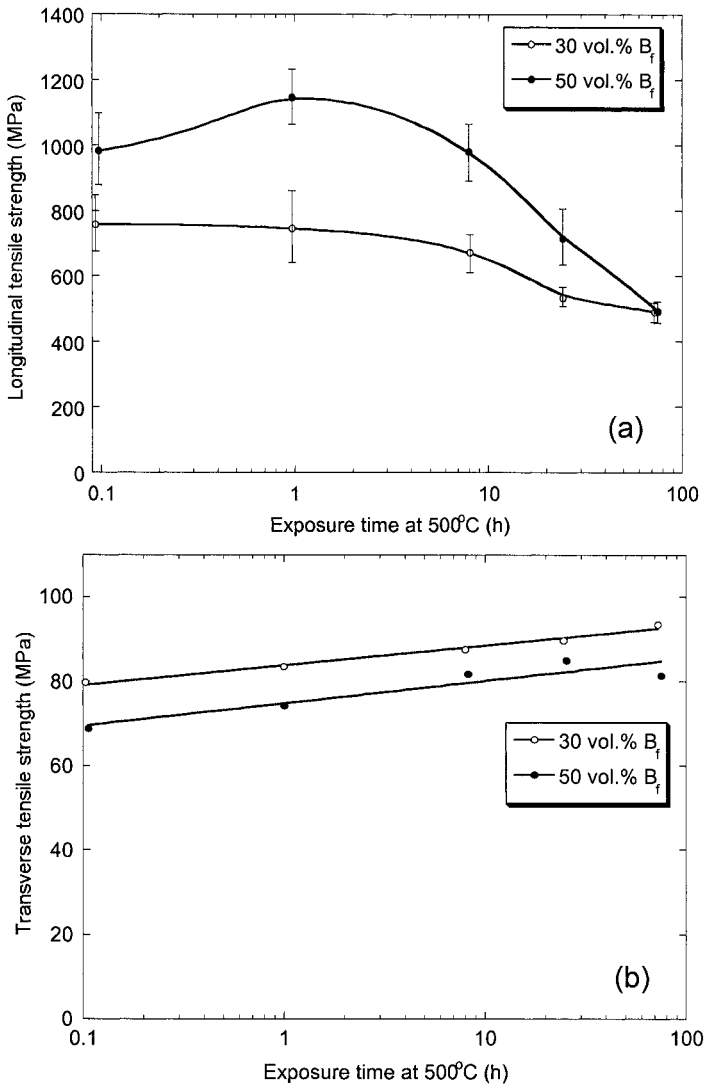
Fig. 7.18 Effect of exposure time at 500°C on the tensile behavior of Al/B_f composites in (a) longitudinal orientation and (b) transverse orientation (after Kyono et al., 1986). AlB_2 is formed at the interface and its thickness increases with exposure time. Circumferential cracks in the brittle interface form during tensile loading along the longitudinal direction. In the transverse orientation, the interface strength increases slightly with exposure time.
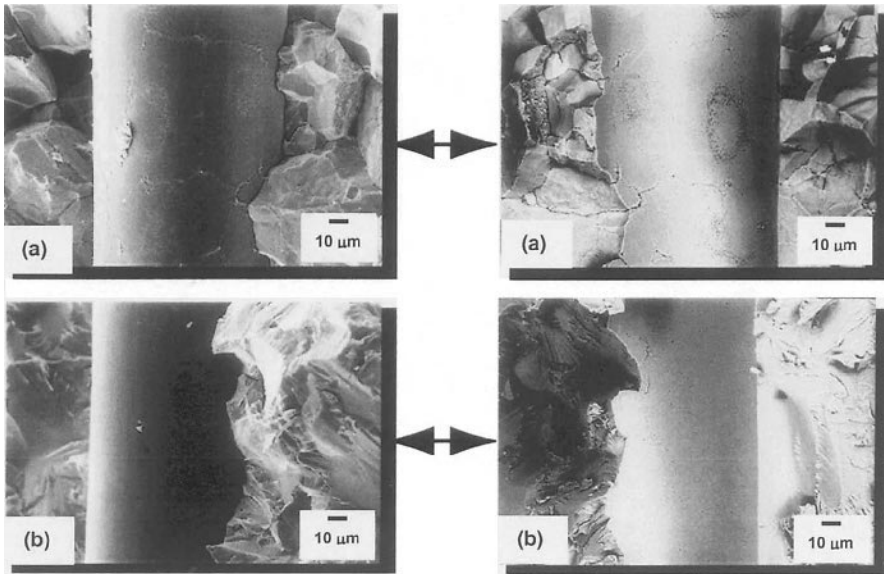
Fig. 7.19 Matching transverse fracture surfaces of sapphire fiber reinforced NiAl matrix composites (after Eldridge et al., 1997; courtesy of J.I. Eldridge): (a) with polymethyl methacrylate (PMMA) binder and (b) without binder (after Eldridge et al., 1997). Composites with the binder exhibited a large amount of carbon residue at the fiber/matrix interface, which prevented a strong interfacial mechanical bond and led to lower interfacial strength.

The extent of interfacial reaction can be reduced by the application of a thin fiber coating. In SiC fiber reinforced W composites, for example, a reaction zone of tungsten silicide is formed, which embrittles the interface and reduces the strength of the composite. Deposition of a TiC coating significantly limited the reduction in strength (Faucon et al., 2001). It should be noted that while the incorporation of a fiber coating may hinder interfacial reaction, it may also contribute to a lower degree of wetting by the matrix and poorer densification of the composite.

As mentioned above, in composites with a precipitation hardenable matrix, the interface may be affected by precipitates in the matrix which typically nucleate heterogeneously at the fiber/matrix interface (see Chapter 3). Cornie et al. (1993) tailored heat treatments to control the precipitate size and spacing at the interface. They found that a minimum in precipitate spacing (which corresponds to a minimum in precipitate size) resulted in a maximum in longitudinal strength and a minimum in transverse strength. This was caused by the decrease in interfacial strength due to precipitation at

the interface. With increasing annealing time, coarsening of the precipitates took place, increasing the precipitate spacing, and increasing the interfacial bond strength. In this case, the transverse strength was maximized, although the longitudinal strength degraded by a small amount. The increase in transverse strength was explained by the increase in the interfacial area fraction of fiber/pure matrix (precipitate-free) bond.

The discussion above points to the difficulty in obtaining a combination of longitudinal *and* transverse strengthening in continuous fiber reinforced MMCs. The longitudinal properties are controlled primarily by the strength and volume fraction of the fibers, while the transverse properties are dictated primarily by the matrix (Rao et al., 1993) and fiber/matrix interface strength (Warrier and Majumdar, 1997). An increase in fiber volume fraction, however, increases the residual stresses during cooling from processing, while also decreases the transverse strength (Rosenberger et al., 1999). Thus, increasing the fiber strength would be a logical step toward increasing the longitudinal strength and simultaneously retaining the transverse properties of the composite. Rosenberger et al. (1999) compared the strength of composites with a high strength ultra-SCS fiber in a Ti alloy matrix, to those with conventional SCS fibers, and showed an increase in longitudinal strength with no corresponding decrease in transverse strength.

Slight changes in composite modulus may also be achieved by controlling the matrix microstructure through heat treatments (Miller and Lagoudas, 2000). This is confined to matrix materials, such as Ti alloys, where a change in crystal structure morphology of second phases takes place during heat treatment. Such manipulation of the matrix microstructure and crystal structure can also be used to tailor composite strength and ductility (Boehlert et al., 1997). In addition, other processing parameters may be used to tailor the matrix microstructure. Blucher et al. (2001) for example, studied the tensile behavior of composite wires of $Al/Al_2O_{3,f}$ (Nextel 610), $6061/Al_2O_{3,f}$, and Al/C_f. With increasing wire drawing velocity, an increase in strength was observed, Figure 7.20. This was attributed to the refinement in the microstructure, due to higher solidification rate, at higher drawing velocity. In the Al/C_f composites, a reduction in interfacial reaction with increasing drawing velocity may have also contributed to the observed behavior.

7.2.4 Modeling of monotonic behavior of continuous fiber reinforced MMCs

The tensile behavior of continuous fiber reinforced MMCs has been modeled extensively by finite element modeling (Brockenbrough et al., 1991; Gonzalez and LLorca, 2001; Rossoll et al., 2005). Gonzalez and LLorca
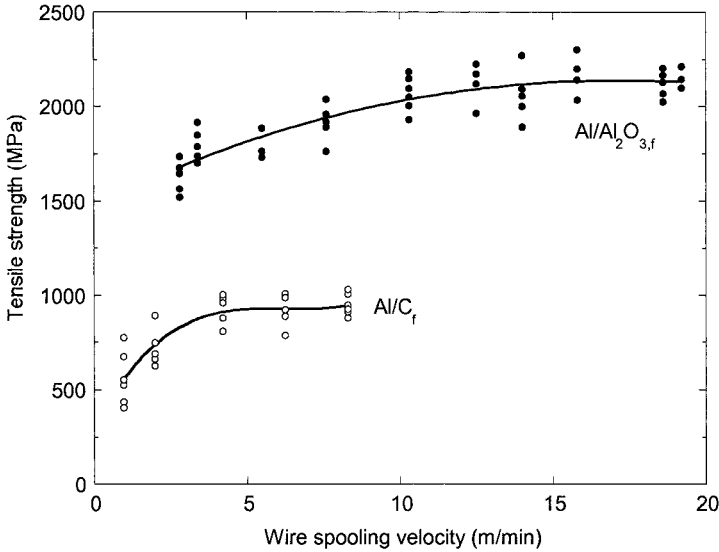
Fig. 7.20 Effect of wire spooling velocity on the tensile strength of $Al/Al_2O_{3,f}$ and Al/C_f composites (after Blucher et al., 2001). Increasing drawing velocity results in faster solidification rate and finer microstructure. In the case of Al/C_f it also reduces the time for interfacial reaction.

(2001) studied the tensile behavior of SCS-6 fiber reinforced Ti-6Al-4V matrix composites at ambient and elevated temperatures. The fibers were modeled using an axisymmetric model shown in Fig. 7.21(a). The fibers are embedded in a "homogeneous composite" with average composite properties. A comparison of the stress-strain behavior predicted by the model with the experiment is shown in Fig. 7.21(b). The experimental behavior is shown as the gray shaded region (due to slight scatter in the data), while the model prediction is shown in the solid black line. The composite exhibited an initial linear portion followed by a pronounced deviation from linearity and fracture of the composite. Note that due to the processing-induced residual stress, at zero applied stress the matrix is in a state of residual tension while the fiber is in compression. With increasing applied stress, the load on both fiber and matrix increase, although the rate of loading in the fiber is higher because of load transfer from the matrix. When the matrix yields, the stress in the matrix reaches a plateau. This stress corresponds to the deviation from linear stress-strain behavior of the composite. The stress in the fiber, on the other hand, continuously increases until fracture of the composite takes place.
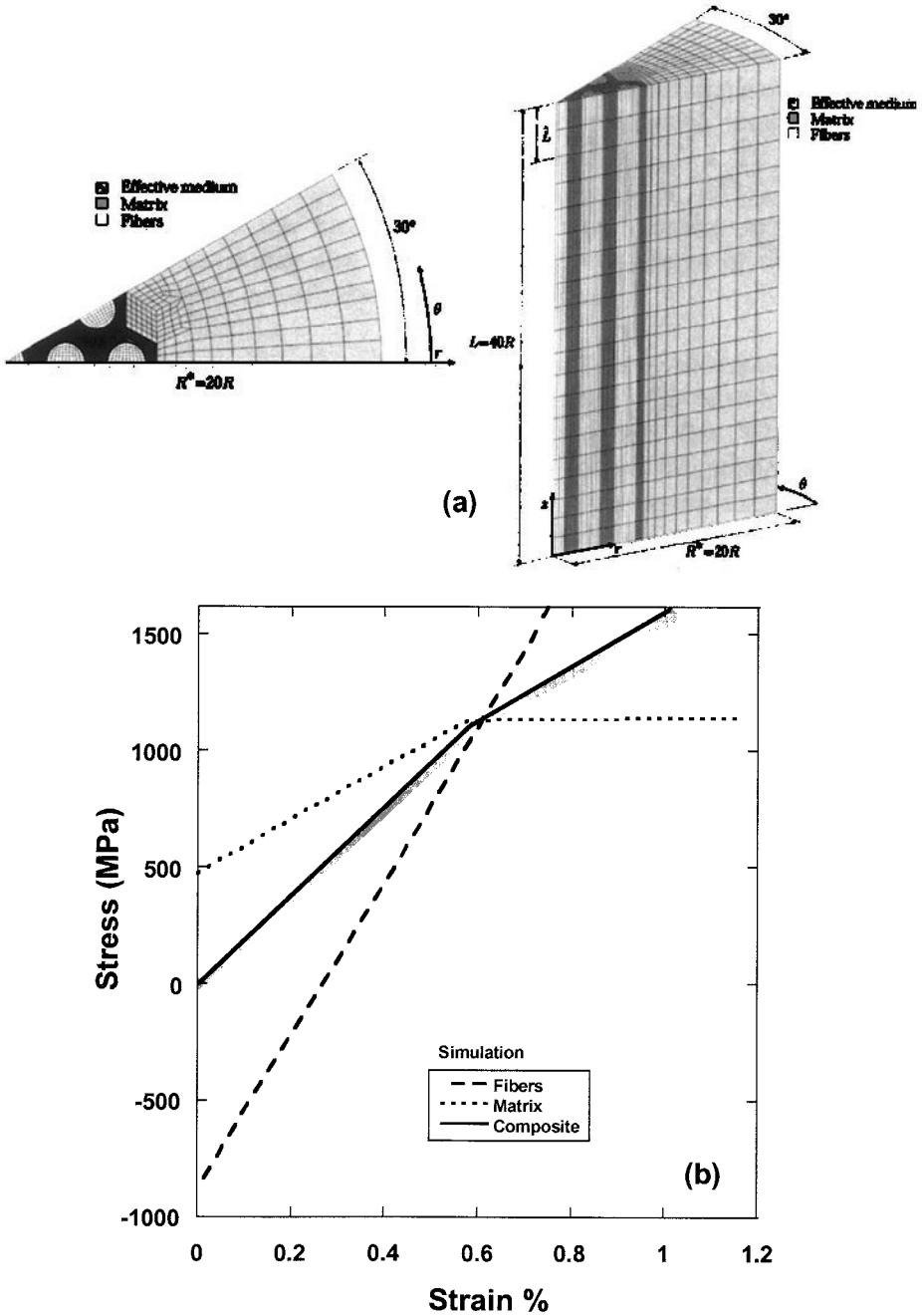
(a)

(b)

Fig. 7.21 Finite element modeling of tensile behavior of fiber reinforced Ti-6Al-4V matrix composites (after Gonzalez and LLorca, 2001; courtesy of J. LLorca): (a) finite element model and (b) simulated composite, fiber, and matrix response. The simulated response correlates well with the experiment.

When a fiber fractures, the stress on neighboring fibers is also affected, since more load is carried by these fibers. The stress state in neighboring fibers is shown in Fig. 7.22. The stress in the neighboring fibers is highest in the plane of fracture of the original fiber. The first-nearest neighbor fiber has the highest stress, followed by the second and third-nearest neighbor, respectively.

As shown above, during longitudinal loading the load is carried primarily by the fibers, although plastic deformation of the matrix between the fibers also takes place. Under transverse loading, however, significant plastic deformation between the fibers takes place. Thus, under transverse loading, the distribution of the fibers plays an important role in the composite response. Brockenbrough et al. (1991) modeled the longitudinal and transverse response of a $6061/B/46_f$ composite with varying fiber distributions. As one would expect, under longitudinal loading, fiber distribution did not have a significant influence on the modeled behavior, Fig. 7.23(a), since the composite behavior was dominated by the response of the fibers. The experimental behavior compared well with the model
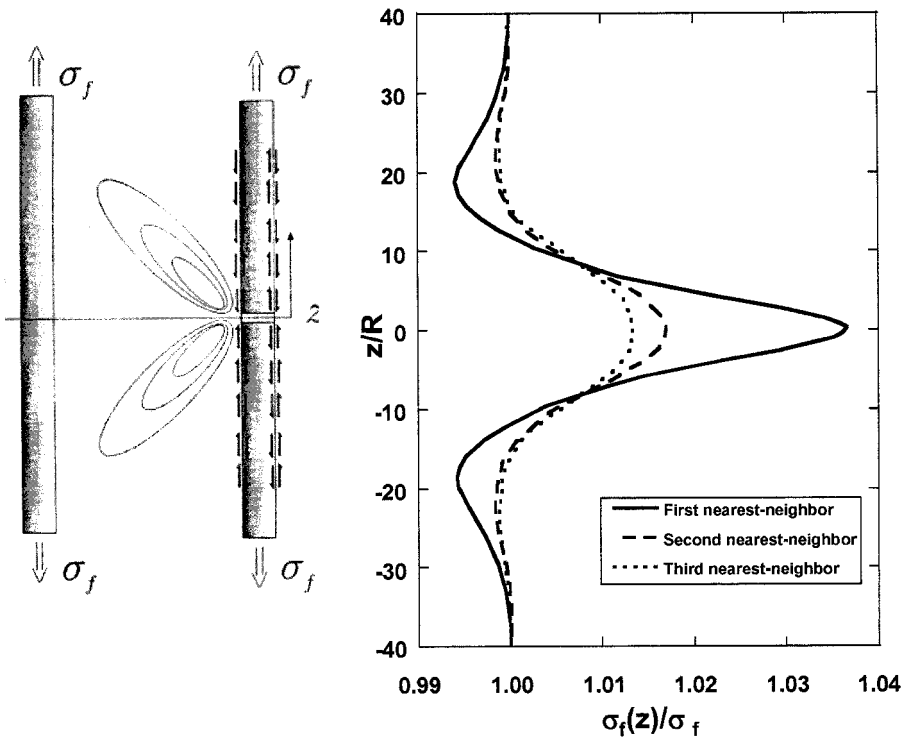
Fig. 7.22 Effect of single fiber fracture on stress state in neighboring fibers, predicted by finite element modeling (after Gonzalez and LLorca, 2001; courtesy of J. LLorca). The stress is highest in the first nearest-neighbor.

prediction. Under transverse loading, the fiber distribution was modeled as square, square-diagonal, and triangle-packed, Fig. 7.23(b). The elastic regime was somewhat unaffected by the fiber distribution. Once the matrix yielded, the effect of fiber distribution became more apparent. The distribution of square packing exhibited the highest work-hardening rate, followed by triangle and square-diagonal packing, respectively.

Rossoll et al. (2005) used finite element analyses (FEA) for varying fiber distributions, ranging from single fiber unit cells to complex cells to study the damage evolution during a tensile test. The *in situ* flow stress of the matrix in the composite was found to be different from that of the unreinforced alloy. This is the result of constrained deformation of the metal matrix in the composite, especially in the presence of clustering of fibers. This results in a deviation from the rule-of-mixtures, based on isostrain, because of a stiffening effect of matrix confinement when surrounded by touching fibers.

7.3 MONOTONIC BEHAVIOR OF DISCONTINUOUSLY REINFORCED MMCS

The monotonic behavior of discontinuously reinforced MMCs is dependent on several factors, such as reinforcement volume fraction, particle size, shape, and matrix microstructure. Chawla et al. (1998a) examined the effect of particle volume fraction (at a constant SiC particle size) on monotonic tensile behavior. Figure 7.24 shows the tensile behavior of an Al-Cu-Mg (2080)/SiC_p-T8 composite with varying volume fraction (at a constant particle size of 5 μm). With an increase in volume fraction, higher elastic modulus, macroscopic yield and tensile strengths, and lower ductility were observed. A comparison of the measured increase in yield strength, with increasing reinforcement volume fraction, compared very well with predictions from a simple modified shear lag analysis by Nardone and Prewo (1989) (see sec. 7.1.1 in this chapter).

As mentioned in section 7.1, microsplasticity takes place at a fairly low stress, which corresponds to the proportional limit stress in the stress-strain curve. This microplasticity originates from stress concentrations at the poles and sharp corners of the particle, Fig. 7.25 (Chawla et al., 1998b). The initial microyielding stress decreases with increasing volume fraction of reinforcement, as the number of stress concentration points increases. The work hardening rate increases with increasing volume fraction of reinforcement (and decreasing matrix volume). The lower ductility can be attributed to the earlier onset of void nucleation with increasing reinforcement. The high stress concentration at the tips of the cracked
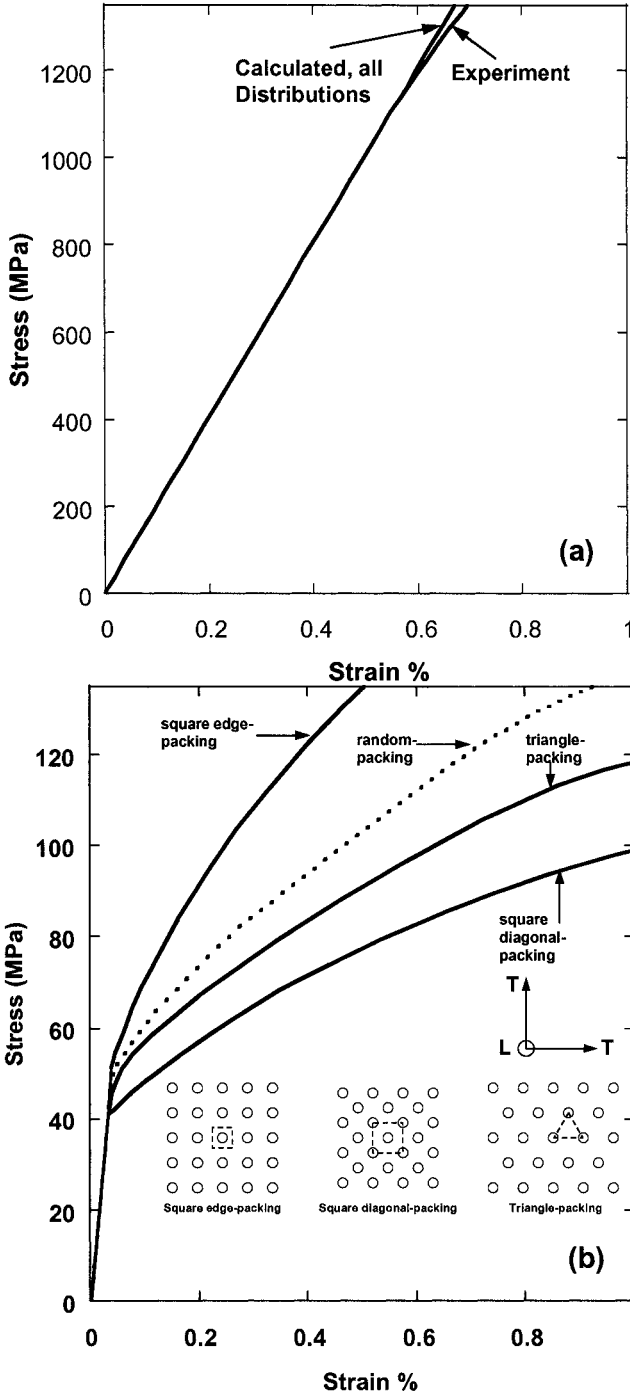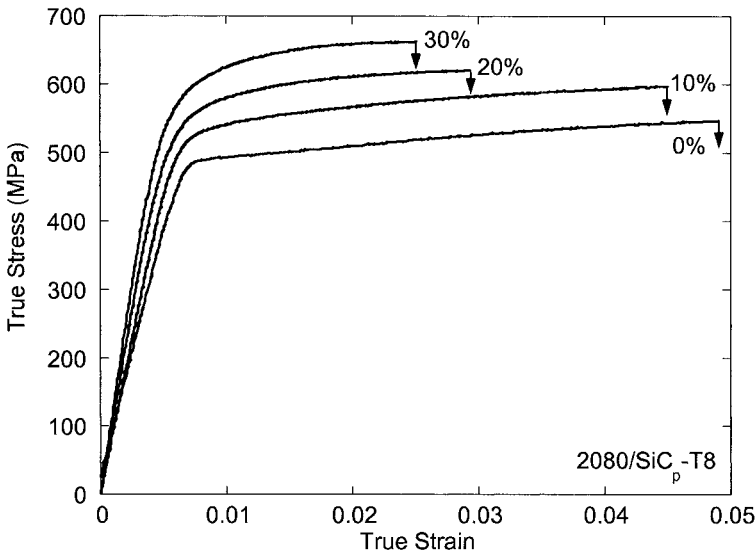
Fig. 7.23 Finite element model predictions of tensile behavior of continuous fiber reinforced composites with varying fiber arrangement (after Brockenbrough et al., 1991): (a) longitudinal and (b) transverse.

Fig. 7.24 Tensile behavior of an Al-Cu-Mg (2080)/SiC$_p$-T8 composite with varying volume fraction, at a constant particle size of 5 μm (after Chawla et al., 1998a). With an increase in volume fraction, higher elastic modulus, macroscopic yield and tensile strengths result, coupled with lower ductility.
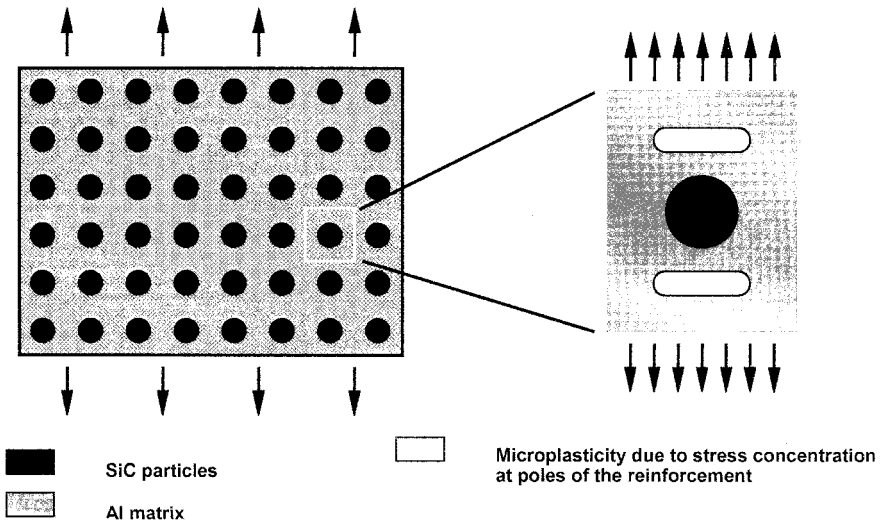

Fig. 7.25 Microplasticity in the matrix of particle reinforced MMCs due to stress concentrations at the poles of the reinforcement and/or at sharp corners of the reinforcing particles (after Chawla et al., 1998b).

particles could also contribute to a lower ductility in the composite, compared to the unreinforced alloy.

The effect of particle size on tensile behavior has been documented by several investigators (Mummery et al., 1991; Manoharan and Lewandowski, 1992; Chawla et al., 1998a). Figure 7.26 shows the general trend of increase in strength and ductility with a decrease in particle size. This may be attributed to an increase in the SiC particle strength with a decrease in particle size. This inverse relationship between particle size and particle strength can be explained as follows. As the volume of the particle increases, the probability of a strength-limiting flaw existing in the volume of the material also increases. At relatively large particle sizes of this material, a significant amount of particle cracking takes place during extrusion prior to testing. Chawla et al. (1998a), showed that in Al 2080/SiC_p composites, with volume fractions ranging from 10 to 30 vol. %, particle cracking was observed above an average particle size of 20 μm. Cracked particles don't carry any load, so the strength of the composite is lower than that of the unreinforced material, Fig. 7.26.

A lower particle size also means a lower interparticle spacing (for a given
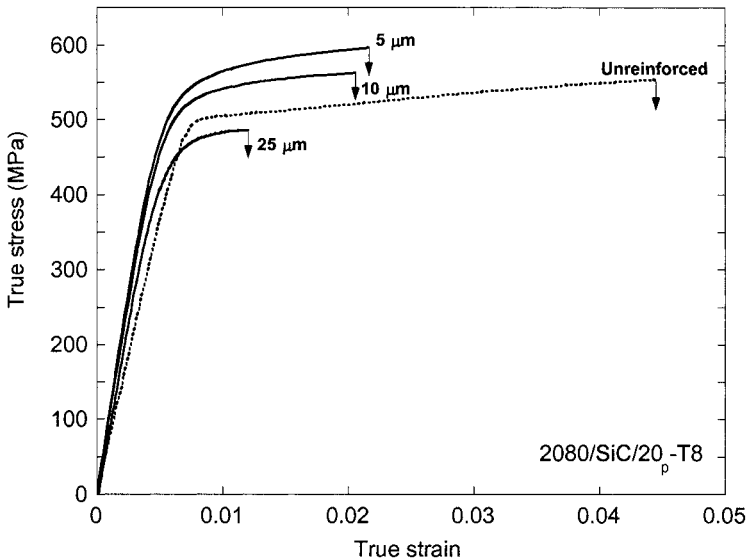
Fig. 7.26 Effect of reinforcement particle size on tensile behavior of an Al-Cu-Mg (2080)/SiC_p-T8 composite, at a constant volume fraction of 20% (after Chawla et al., 1998a). Very large particles are detrimental to strength because of processing-induced fracture, prior to testing. Above about 20 μm or so, strength and ductility both increased with decreasing particle size.

volume fraction of particles) so that nucleated voids in the matrix are unable
to coalesce as easily (Mummery et al., 1991). A higher work hardening rate
has also been observed with decreasing particle size (Lewandowski et al.,
1991; Manoharan and Lewandowski, 1992). This is attributed to the
formation of dislocation tangles around the particles and the formation of a
dislocation cell structure with a cell size directly proportional to the
interparticle spacing (Kamat et al., 1989).

The fracture of particle reinforced MMCs is very much dependent on
particle strength and particle/matrix interface strength. A schematic of the
two possible types of damage evolution is shown in Fig. 7.27. If the strength
of the interface is greater than the particle strength (often observed in peak-
aged composites) then the particles fracture before the interface. Matrix void
growth takes place, and shear localization between fractured particles results
in failure of the composite. In order to quantify the extent of particle fracture
and particle pullout during tensile loading, both mating fracture surfaces
need to be examined. An example of mating fracture surfaces is shown in
Figure 7.28. A particle found on both mating fracture surfaces has fractured.
The nature of fracture of the brittle SiC particles is quite interesting. Figure
7.29 shows the fractured surface of a SiC particle after tensile loading. Note
the spherical flaws or voids on the fracture surface, which presumably were
responsible for crack initiation in the particles. The flaws arise during
processing of the particles. The second scenario for damage is when the
interface strength is much lower than the particle strength. Here, void
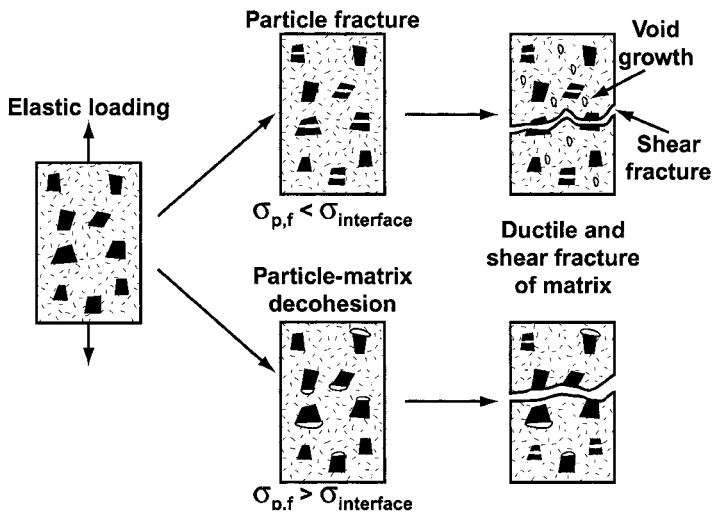
Fig. 7.27 Schematic of the two possible types of tensile damage evolution in
particle reinforced MMCs: (a) interface strength greater than particle
strength and (b) interface strength less than particle strength.
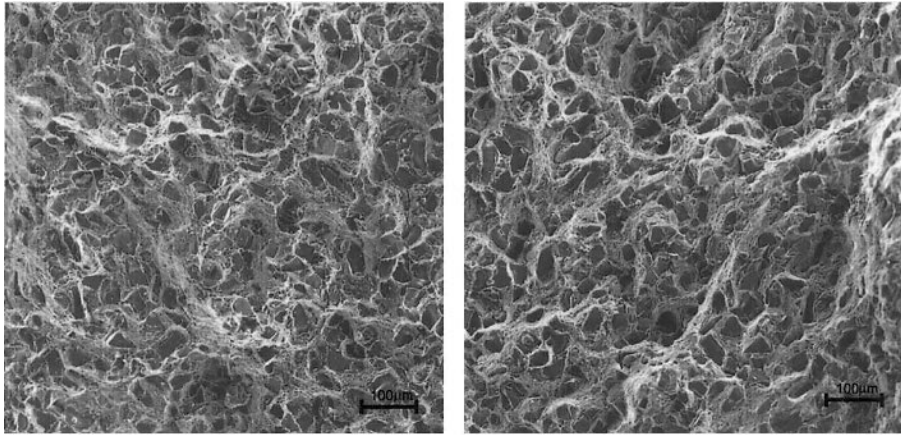
Fig. 7.28 Mating tensile fracture surfaces of a 2080/SiC/20p composite showing significant amount of particle fracture (after Chawla et al., 2002a).
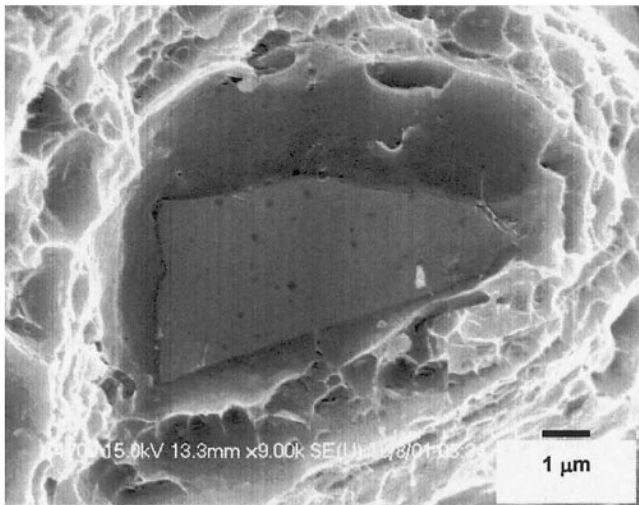
Fig. 7.29 Fracture surface of a SiC particle after tensile loading (after Chawla et al., 2002b). Note the spherical flaws or voids on the fractured particle surface, which presumably are responsible for crack initiation. The flaws arise during processing of the particles.

nucleation and growth will take place at the interface, due to decohesion of the matrix from the particle. This will be followed by ductile shear fracture through the matrix alone. An example of this is shown in Figure 7.30, for an overaged composite, with relatively weak interface strength. Note that a thin matrix layer has been left on the SiC particle surface.

Particle reinforced composites, especially those subjected to extrusion,
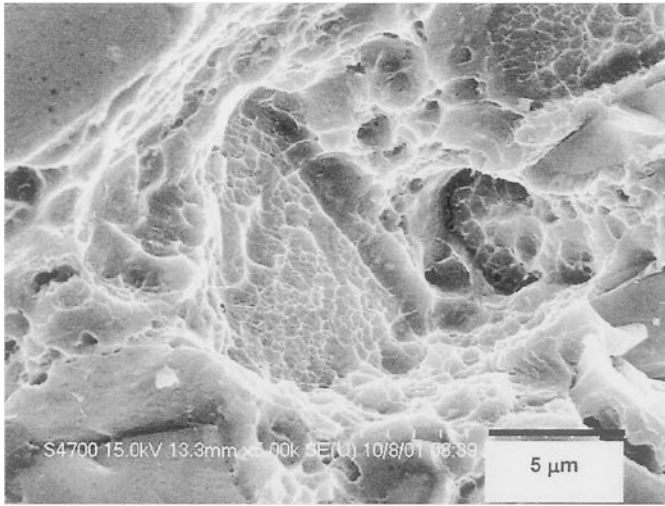
Fig. 7.30 Void nucleation and growth at the particle/matrix interface, due to relatively weak interface strength (overaged condition). Ductile shear fracture is also observed in the matrix of the composite (after Chawla et al., 2002b).

exhibit a fair amount of anisotropy due to preferential particle orientation along the extrusion axis. Logsdon and Liaw (1986) studied the tensile strength anisotropy behavior in SiC particle and whisker reinforced aluminum alloys, and noted that the strength was higher parallel to the extrusion axis, than perpendicular to the extrusion axis. Jeong et al. (1994) also noted a higher Young's modulus of the composite along the extrusion axis. Ganesh and Chawla (2004, 2005) noted that the extent of orientation was highest for lowest volume fraction composites, since with increasing volume fraction the mean free path for rotation and alignment of a given particle decreased. The Young's modulus and tensile strength of the composites, independent of orientation, increased with increasing volume fraction of reinforcement, Fig. 7.31. Thus, although the degree of microstructural anisotropy was greatest for $2080/SiC/10_p$, the greatest anisotropy in mechanical behavior was observed in $2080/SiC/30_p$.

The mechanical properties of lower cost processing techniques, such as sinter-forging, have been compared to existing hot-pressed and extruded materials. Chawla et al. (2002a) examined the strength of composites fabricated by a low-cost sinter-forging approach. The SiC particle size was relatively coarse, e.g., 25 μm. Materials processed by the sinter-forged approach exhibited similar tensile properties to those of the extruded material of similar composition, reinforcement volume fraction, and particle size, Fig. 7.32. The microstructure of the sinter-forged composites exhibited relatively uniform distribution of SiC particles, which appeared to be
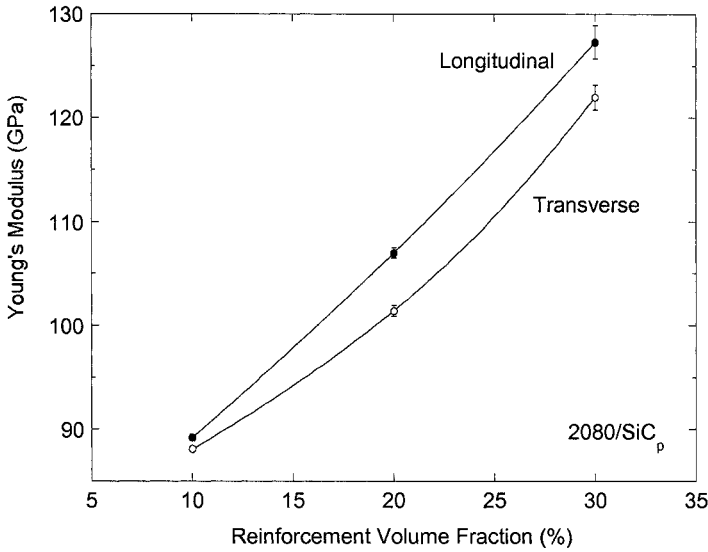
Fig. 7.31 Anisotropy in Young's modulus in a 2080/SiC$_p$ composite (after Ganesh and Chawla, 2005). The longitudinal orientation is parallel to the extrusion axis, while transverse is perpendicular.
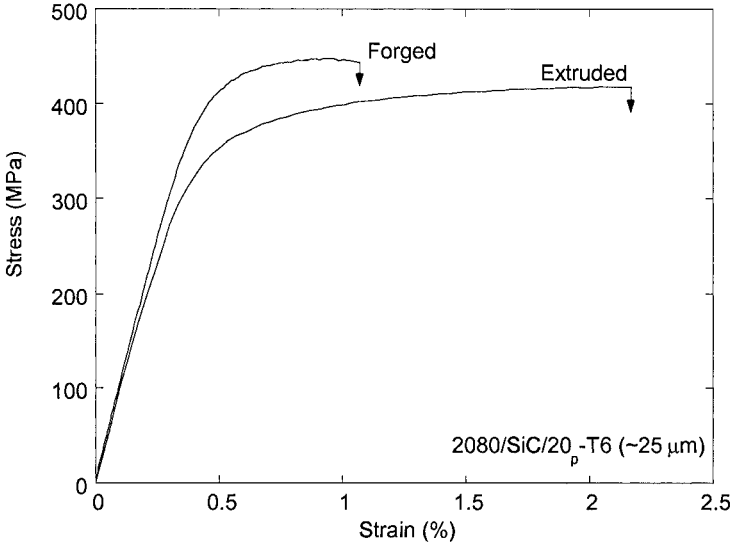

Fig. 7.32 Tensile strength of 2080/SiC/20$_p$-T6 fabricated by low-cost sinter-forging and extrusion approach (after Chawla et al., 2002a). The sinter-forged material exhibited similar tensile properties, with slightly lower ductility, than the extruded material.

somewhat aligned perpendicular to the forging direction. The degree of alignment and interparticle bond strength was not as high as that observed for the extruded composite. The sinter-forged composite exhibited higher Young's modulus and ultimate tensile strength than the extruded material, but lower strain-to-failure. The higher modulus and strength were attributed to the absence of any significant processing-induced particle fracture, while the lower strain-to-failure was caused by poorer matrix interparticle bonding compared to the extruded material. Indeed, secondary working of the composite, such as extrusion after initial casting, can significantly improve the ductility of the composite, Fig. 7.33 (Lloyd, 1997). The ductility of the composite is also very much a function of the degree of particle clustering. Murphy et al. (1998) controlled the degree of particle clustering by controlling the cooling rate of the composite. The degree of particle clustering was measured by tesselation techniques (see inset), to determine a clustering severity parameter, P. The ductility of the composite was found to significantly decrease with increasing P.

Matrix microstructure also plays an important role on strength of the composite. Overaging heat treatments modify the matrix microstructure, resulting in coarsening of the precipitate structure, while retaining a homogeneous precipitate distribution, which directly influences the strength
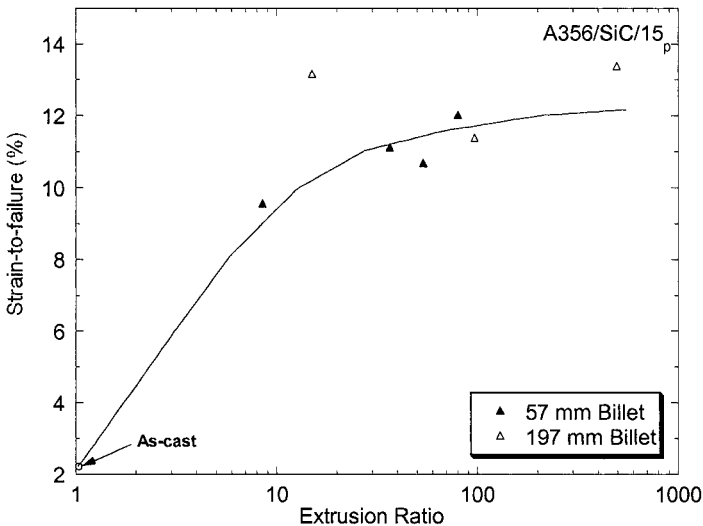

Fig. 7.33 Effect of degree of secondary working (i.e., extrusion ratio) on ductility of Al/SiC/15$_p$ (after Lloyd, 1997). Extrusion significantly improved the ductility of the composite.

Quantifying Reinforcement Clustering

During processing of continuous fiber or particle reinforced MMCs, clustering of the reinforcement is likely to take place (see chapter 4). While individual fibers can be distributed relatively homogenously (e.g., when woven in a fiber fabric), controlling particle distribution can be more challenging. As shown in this chapter, reinforcement clusters have a profound effect on mechanical properties, because the clusters act as stress concentrations. Many techniques have been used to quantify the degree of reinforcement clustering. Here we describe two techniques that can be used to obtain some measure of reinforcement clustering: (a) Dirichlet and finite-body tessellation and (b) digital image dilation.

The technique is name after the mathematician Dirichlet (1850) who proposed a tessellation scheme to quantify the arrangement of geometric objects in space. Consider a hypothetical two-dimensional microstructure consisting of elliptical particles in space (see figure below). Let us mark the centroid of each ellipse. We can now construct cells around the particles, such that each cell wall is equidistant between two centroids (part (b) in the figure below). This construction is called a tessellation. The tessellation is very useful because it yields information about the cell size, nearest-neighbor spacing distributions between particles, etc. Inspection of the Dirichlet tessellation, however, shows that when the objects are not perfect spheres (in this case ellipses), the particles are not always fully contained within the cell boundaries. This is because the centroid of the ellipse is used to construct the tessellation. Thus, for the case of non-spherical reinforcement, a conventional tessellation is not quite adequate for quantifying the microstructure.
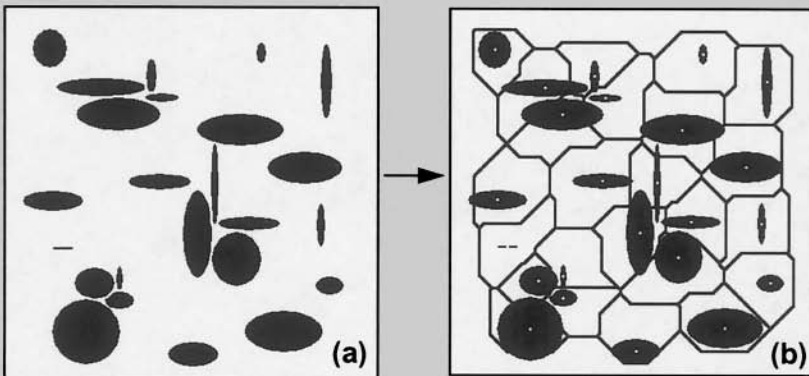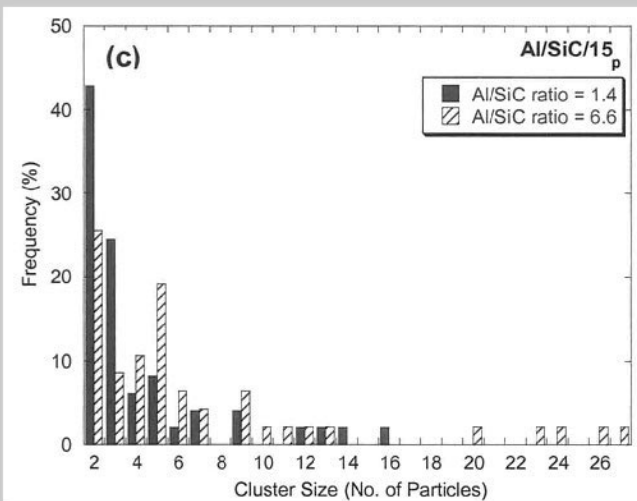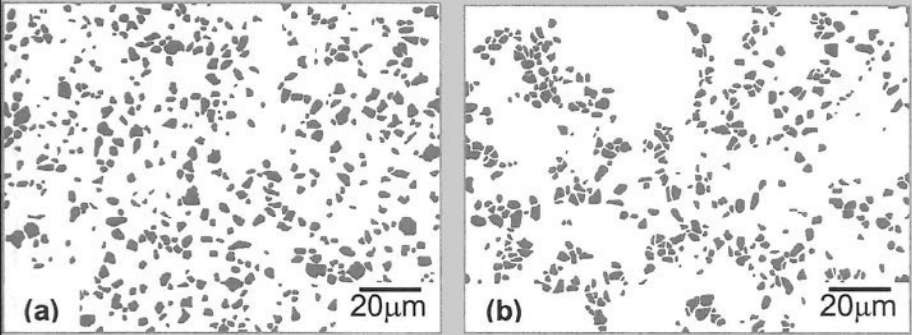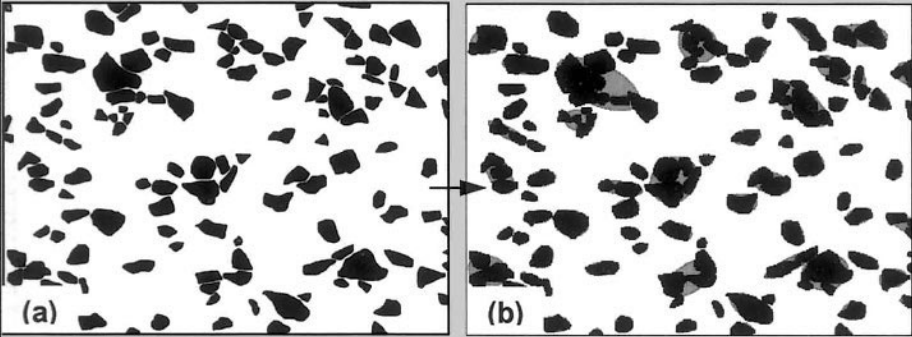
The conventional tessellation scheme can be enhanced by employing a finite body tessellation (Chawla et al., 2002a). The steps involved in this process are shown in the panel below. An optical or scanning electron micrograph, (a), is segmented into a black and white image, (b). A watershed image operation is then conducted, (c), which analyzes distances between particles based on the centroid and perimeter of each particle. A tessellation is then constructed, (d), whereby each of the irregular particles resides within the boundaries of the cell. Similar statistics can be obtained from the finite body tessellation as those from the conventional tessellation.
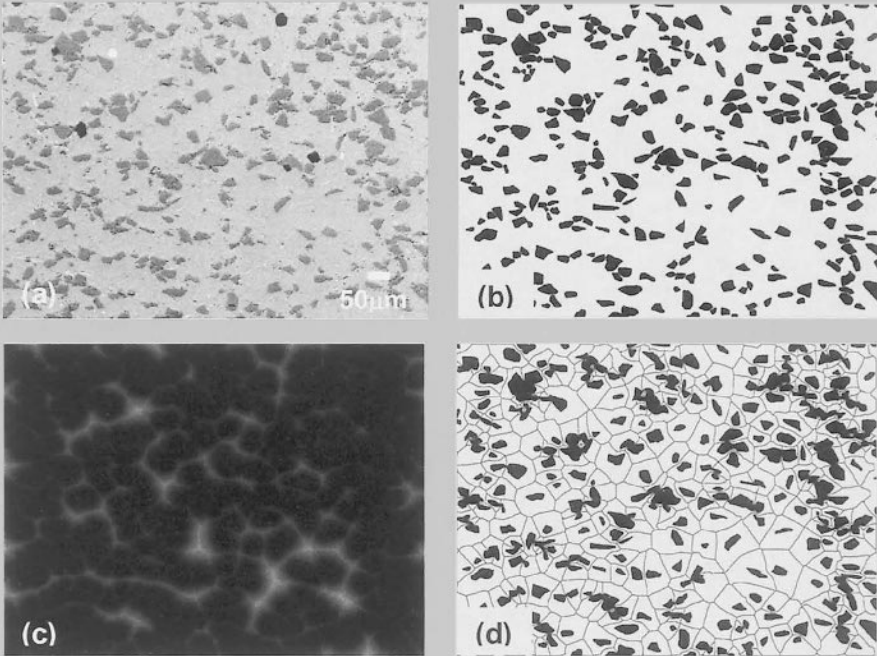
An alternative method for quantifying the degree of clustering in a composite is to use a digital image dilation technique (Chawla et al., 2002a). This technique consists of, again, analyzing a segmented microstructure (part (a) below). The perimeter of each particle is "dilated" by a certain increment, part (b). The dilation increment can be calculated by analytical expressions for the average interparticle spacing for a random distribution of particles of single (Meyers and Chawla, 1999) or multiple sizes (Torquato, 2002). If the particles are touching after the dilation, then this set of particles is identified as a cluster (shaded region in part (b)). The cluster may be quantified by the number of particles in the cluster or by the area fraction of the cluster, relative to the whole microstructure. Ayyar et al. (2005) used this technique to show the relative degree of clustering between two microstructures (also shown below). The microstructure on the left is

relatively homogeneous and the one on the right is highly clustered. Part (c) shows a histogram of the cluster size distribution for the two microstructures. Note that the clustered microstructure has a much higher fraction of larger clusters. This information is particularly useful from a cyclic fatigue design perspective, since the fatigue life is controlled by the largest defect (cluster) size.

(a)

(b)

(a)   20μm

(b)   20μm

(c) Al/SiC/15$_p$

- ■ Al/SiC ratio = 1.4
- ▨ Al/SiC ratio = 6.6

Frequency (%) vs Cluster Size (No. of Particles)

of the composite (Chawla et al., 2000). Figure 7.34 shows the coarsening and increase in precipitate spacing in the matrix of MMCs overaged at various temperatures for 24 h. Increasing precipitate spacing decreases tensile strength, Fig. 7.35. This is to be expected since coarser precipitates result in a larger interprecipitate spacing and easier bypass of dislocations. For the composites subjected to higher overaging temperatures, the yield strength also decreased with an increase in precipitate spacing.

7.3.1 Modeling of Monotonic Behavior of Particle Reinforced MMCs

Similar to modeling of continuous fiber reinforced MMCs, FEM modeling has also been used to model the behavior of discontinuously reinforced MMCs. Figure 7.36(a) shows several single particle unit-cell models, in which the left vertical boundary represents the axially symmetric axis and mirror symmetry exists about the horizontal boundary. A periodic arrangement of particles with the shape of a "unit cylinder," "truncated cylinder," "double-cone," and "sphere" may be simulated using the appropriate boundary conditions (Shen et al., 1994). The matrix is modeled as an isotropically hardening elastic-plastic solid (following the experimental stress-strain curve of a peak-aged Al-3.5Cu alloy) and the SiC particles as an elastic solid. The calculated tensile stress-strain response of Al/SiC/20$_p$ composites, having the four particle shapes described above, is shown in Fig. 7.36(b). Clearly, particle shape has a significant influence on the overall tensile behavior of the composite. The unit-cylinder particles clearly strengthen the composite more than the other three shapes for a given reinforcement fraction. This, however, does not imply that particles with sharp corners have a more pronounced strengthening effect, as shown by the case of "double-cone" particles, possessing the "sharpest" type of corners. A detailed analysis (Shen et al., 1995) showed that the unit-cylinder and double-cone particles result in the highest and lowest degrees of "disturbance" of the local plastic flow paths in the matrix, respectively. This directly reflects the different extents of constrained plastic flow and hence the strengthening behavior in the composite. The reader is referred to other simple unit-cell approaches focusing on various aspects of elasto-plastic behavior of short fiber and particle reinforced composites, such as reinforcement particle fracture (LLorca, 1995; Steglich et al., 1999), reinforcement clustering (Christman et al., 1989; Toda et al., 1998), matrix void growth (LLorca et al., 1991), and residual stress from thermal treatments and processing (Levy and Papazian, 1991; Dutta et al., 1993).

The thermal expansion mismatch between the reinforcement and the matrix results in thermal stresses within the composite upon cooling from the
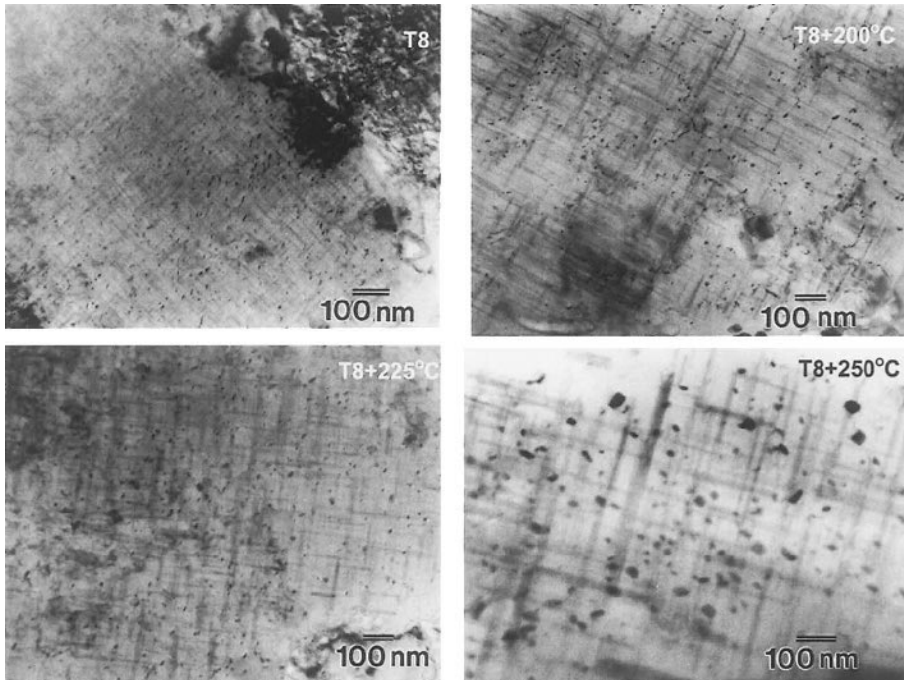
Fig. 7.34 Coarsening and increase in precipitate spacing in the matrix of 2080/SiC/20$_p$-T8 overaged at various temperatures for 24 h (after Chawla et al., 2000).
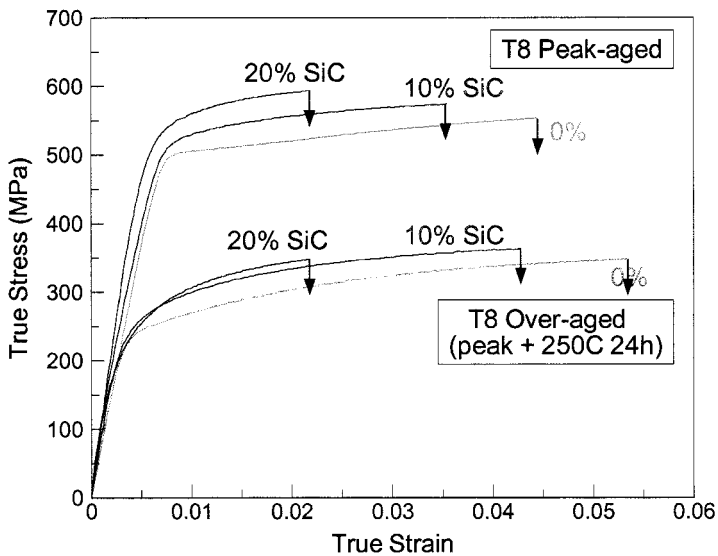
Fig. 7.35 Decrease in strength due to overaging of 2080-T8 and 2080/SiC$_p$-T8 composites (after Shen and Chawla, 2001). The reduction in strength is similar for all materials. Coarser precipitates result in a larger interprecipitate spacing and easier bypass by dislocations.

processing temperature to ambient temperature. As mentioned above, in actual composites thermal residual stresses are relieved by plastic deformation in the matrix, resulting in indirect strengthening. Figure 7.37 shows the calculated tensile stress-strain curves for 20% SiC reinforced Al alloy utilizing the unit-cylinder particles (Fig. 7.36(a)), with and without the presence of thermal residual stress. As before, the matrix was taken to be an isotropically hardening elastic-plastic material in the model. The thermal residual stresses were calculated for a composite cooled from the solutionizing temperature of 500°C, where the composite is in a relatively stress-free state, to room temperature, 20°C. Also included in the figure is the stress-strain response used for the pure matrix. During cooling the matrix near the particle/matrix interface undergoes yielding. This has direct bearing on subsequent loading of the material. It can be seen in Fig. 7.37 that in the presence of thermal stresses a smaller slope is observed at the early stage of deformation, due to the slightly smaller apparent modulus arising from prior plastic deformation. When compared with the material free of residual stresses, higher values of the average axial stress were observed. This means that the existence of residual stresses enhanced the initial strain hardening rate in the material. Comparing the curves for the pure matrix and for the composite without thermal residual stresses, direct strengthening effects are observed. The higher flow stress for the composite is a direct consequence of load transfer from the matrix to the reinforcement, which is also related to the constrained plastic flow within the matrix. A comparison of the two curves of the composite reveals the indirect strengthening effect. In the model strain hardening caused by cooling-induced plasticity leads to subsequent higher strength for the composite with thermal stresses incorporated (after the crossover point). In actual materials thermal mismatch-induced dislocation punching renders higher matrix strength due to strain hardening. Thus, when appropriate constitutive models are chosen (e.g., hardening plasticity rather than perfect plasticity in the present case), continuum-based numerical modeling can provide insights into the deformation mechanisms.

Simple shaped single particle and multiparticle models can provide useful insight into deformation. Microstructure-based models, however, more accurately predict the deformation behavior of the composites (Chawla et al., 2003; Chawla et al., 2004; Ganesh and Chawla, 2004). This is because in actual composites the particles are highly irregular in shape and commonly contain sharp corners, so spherical particles are not necessarily a realistic choice for simulation. Thus, while simplifications in unit cell models may aid in computation, they fail to capture the complex morphology, size, and

(a)
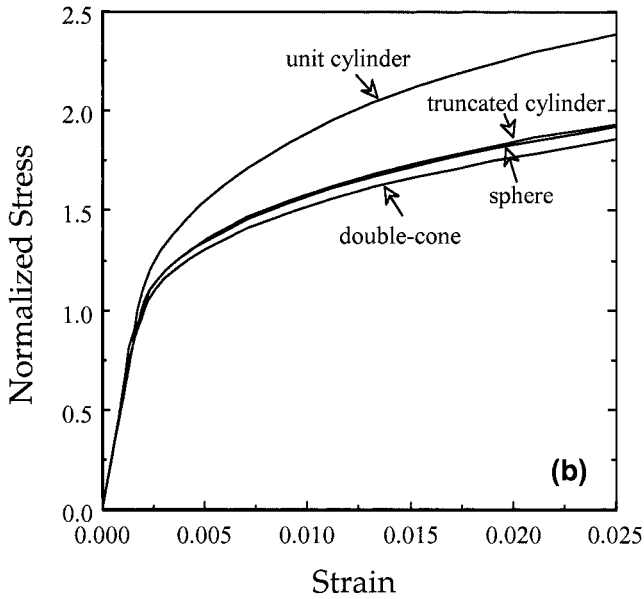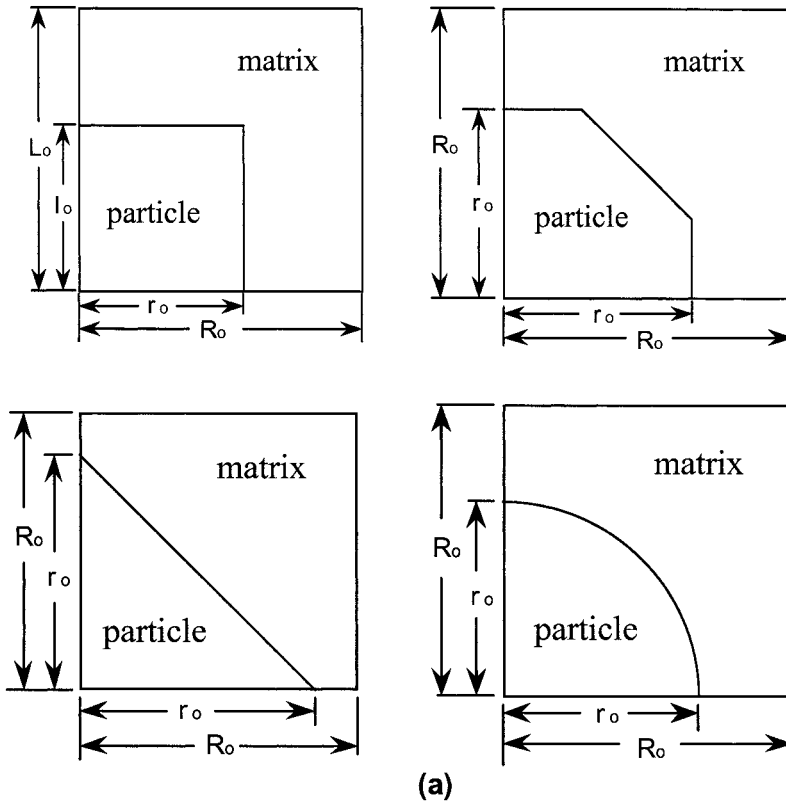
Fig. 7.36 (a) Unit-cell finite element models used to illustrate the effect of particle shape and (b) predicted stress-strain behavior (after Shen et al., 1994).
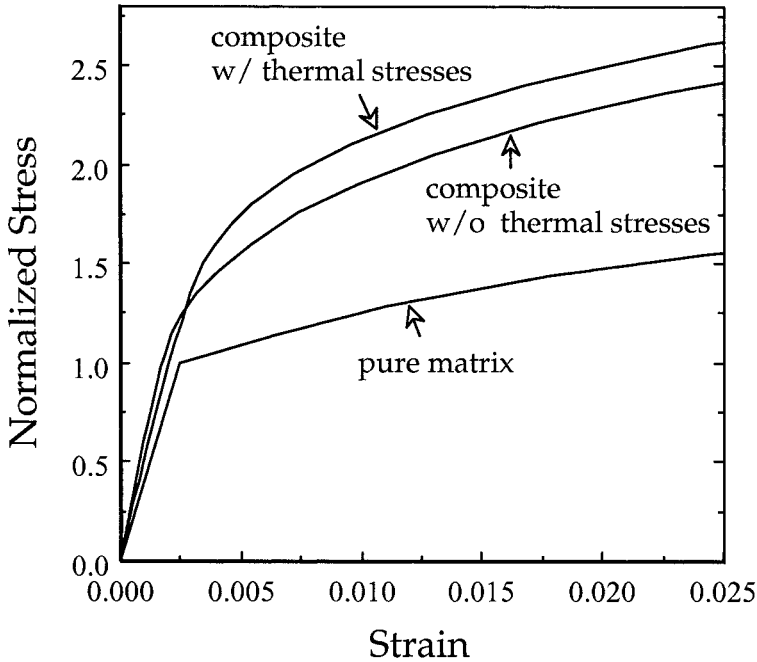
Fig. 7.37 Tensile stress-strain curves for Al/SiC/20$_p$ utilizing the unit-cylinder particles with and without thermal residual stress (after Shen et al., 1994). Hardening caused by cooling-induced plasticity leads to higher strength for the composite.

spatial distribution of the reinforcement. It follows that an accurate simulation of the mechanical behavior of material can only be obtained by incorporating actual three-dimensional (3D) microstructure morphologies as a basis for the model.

A comparison of the modeled 3D response using the actual microstructure versus a simplified representation of spherical particles is shown in Fig. 7.38. The spatial distribution of the particles in both models is about the same. Note that the angular particles are under a much larger stress than the spherical particles, indicating more load transfer to the angular particles. The stress in the spherical particles is quite uniform, while that in the angular particles is not. The plastic strain contours in the matrix are also quite different. More localization of strain is observed in the model with angular particles. This simple comparison shows that, indeed, the microstructure-based model predictions are quite different from those of simplified spherical particles. Thus, modeling of the material using the actual microstructure is extremely important.
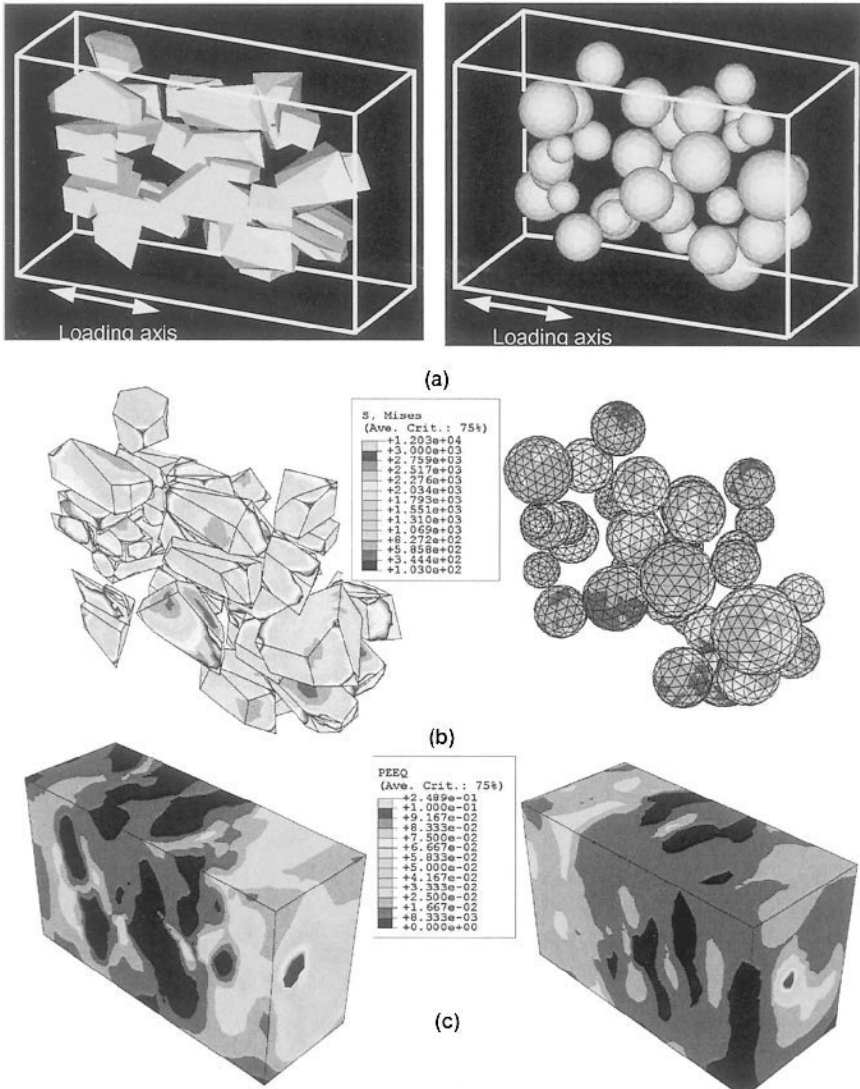
Fig. 7.38 Comparison between 3D finite element models incorporating (i) actual microstructure and (ii) approximation to spherical particles: (a) FEM models, (b) stress distribution in particles, and (c) plastic strain in matrix. Note that the microstructure model exhibits much higher stress in the particles and larger and more inhomogeneous plastic strain than the simplified spherical particle model.

A comparison of Young's modulus predicted by unit cell models versus the microstructure-based model was shown in chapter 6. The microstructure-based model was closest to the experiment (Chawla et al., 2004). A comparison of the overall stress-strain curve (elastic and plastic parts) of the 3D microstructure simulation to the experiment is shown in Fig. 7.39. These simulations incorporate a cooling step in the model, from the solution treating temperature of 493°C to 25°C. The prismatic rectangle and microstructure-based models both predict the experimental behavior quite well. Nevertheless, the microstructure-based models more faithfully represent the experimental behavior. More importantly, the localized plasticity that results from the sharp and angular nature of SiC particles, can only be captured in the microstructure-based model. Thus, other models that approximate the shape of the particles to ellipsoids underestimate the extent of strengthening.

The effect of particle clustering has also been modeled using FEM. Segurado et al. (2003) conducted 3D finite element simulations of clustered composites. They showed that within a particle cluster, the stresses in the particles are much higher than the average particle stress, Fig. 7.40(a). With an increase in particle clustering, the standard deviation of the particle stress increased significantly, Fig. 7.40(b). In a practical sense, this would cause
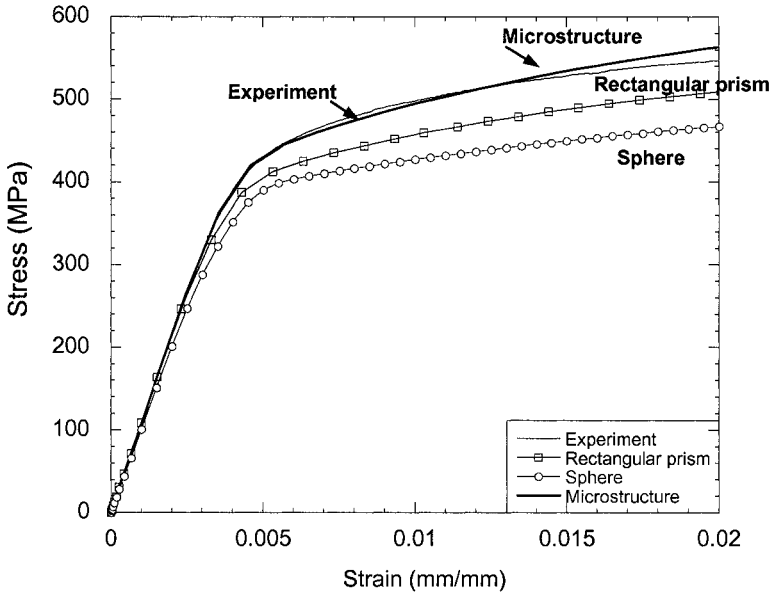

Fig. 7.39 Comparison of stress-strain predictions from various FEM models after cooling (after Chawla et al., 2004). The 3D microstructure model (from two random regions in the microstructure) is most accurate in predicting the experimentally observed behavior.

particle fracture at a much lower far-field applied stress, Fig. 7.40(c) compared to a composite with homogeneous distribution.

Deng and Chawla (2005) developed model microstructures, consisting of circular reinforcement particles in a metallic matrix. The microstructures had varying degrees of particle clustering, as quantified by the coefficient of variance in particle spacing (see inset). The tensile behavior of the microstructure was modeled using two-dimensional (2D) finite element analysis. Matrix plasticity and particle fracture were explicitly modeled. All the particles had a homogeneous strength of 1 GPa. The plastic strain distribution in the matrix is much more homogeneous in the homogeneous particle arrangement, Fig. 7.41(a), although the plastic strain is intensified in the region of particle fracture. In the clustered particle microstructure, larger stresses develop which results in particle fracture within the cluster, Fig. 7.41(b). A lower degree of plastic strain is observed. The modeled stress-strain response shows that the clustered microstructure has a lower "ductility," although matrix fracture was not modeled. This model verifies the experimental results of Murphy et al. (1998), described above.

Shen and Chawla (2001) and Shen et al., (2001) explored the correlation between macro-hardness and tensile properties of particle-reinforced metal matrix composites. It was shown that, unlike most monolithic metals and alloys, hardness does not necessarily scale with the overall strength of particle-reinforced metal matrix composites, Fig. 7.42. The hardness test may significantly overestimate the overall tensile and yield strengths of composites containing large reinforcement particles, which are prone to fracture during deformation processing and/or tensile loading. The predominant local compressive stress state in a hardness test prevents the pre-existing fractured particles from weakening the material during indentation. For composites having relatively small reinforcement particles, a unique relationship between hardness and tensile/yield strength did not exist, even when the material was essentially free of pre-existing fractured particles. This was especially true in cases where the strength of the Al matrix was relatively low. The tendency of higher hardness for particle-reinforced composites can be attributed to the localized increase in particle concentration directly underneath the indenter during hardness testing, Fig. 7.43. This was illustrated by micromechanical modeling using the finite element method. Under indentation, the material system with discrete particles exhibits a higher resistance to deformation than the homogenized system having exactly the same overall stress–strain behavior, Fig. 7.44 (Shen et al., 2001). These findings are true even when the particle size is
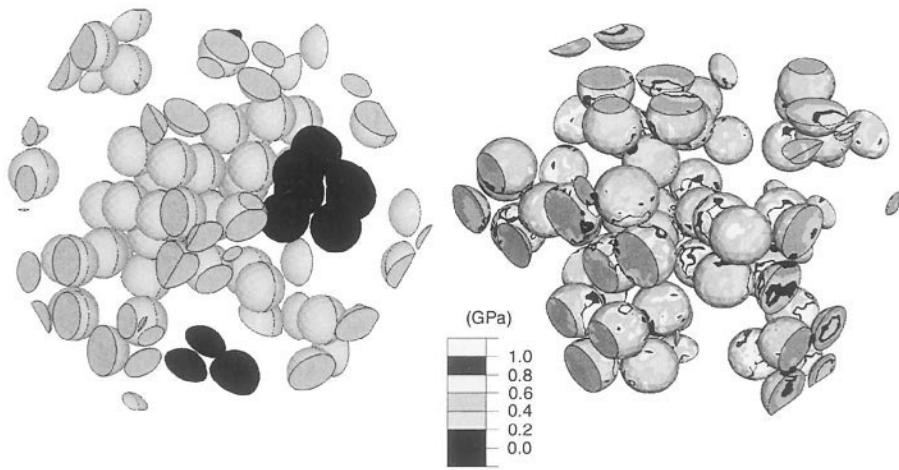
(a)
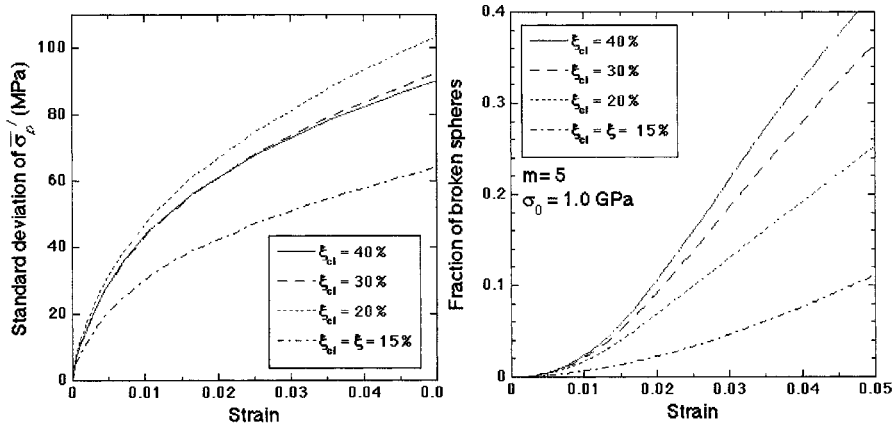
(b)

(c)

Fig 7.40 (a) 3D finite element model consisting of perfectly spherical SiC particles in an Al matrix (after Segurado et al., 2003; courtesy of J. LLorca). The model consists of 49 particles and 7 "clusters." The stress within the cluster is higher than the average stress. (b) Standard deviation of stress in particles with increasing clustering, for a given strain, and (c) fraction of broken particles predicted. ξ and ξ_{cl} are the volume fraction of particles (15%) in the composite and within the cluster, respectively.

(a)

PEEQ

(b)
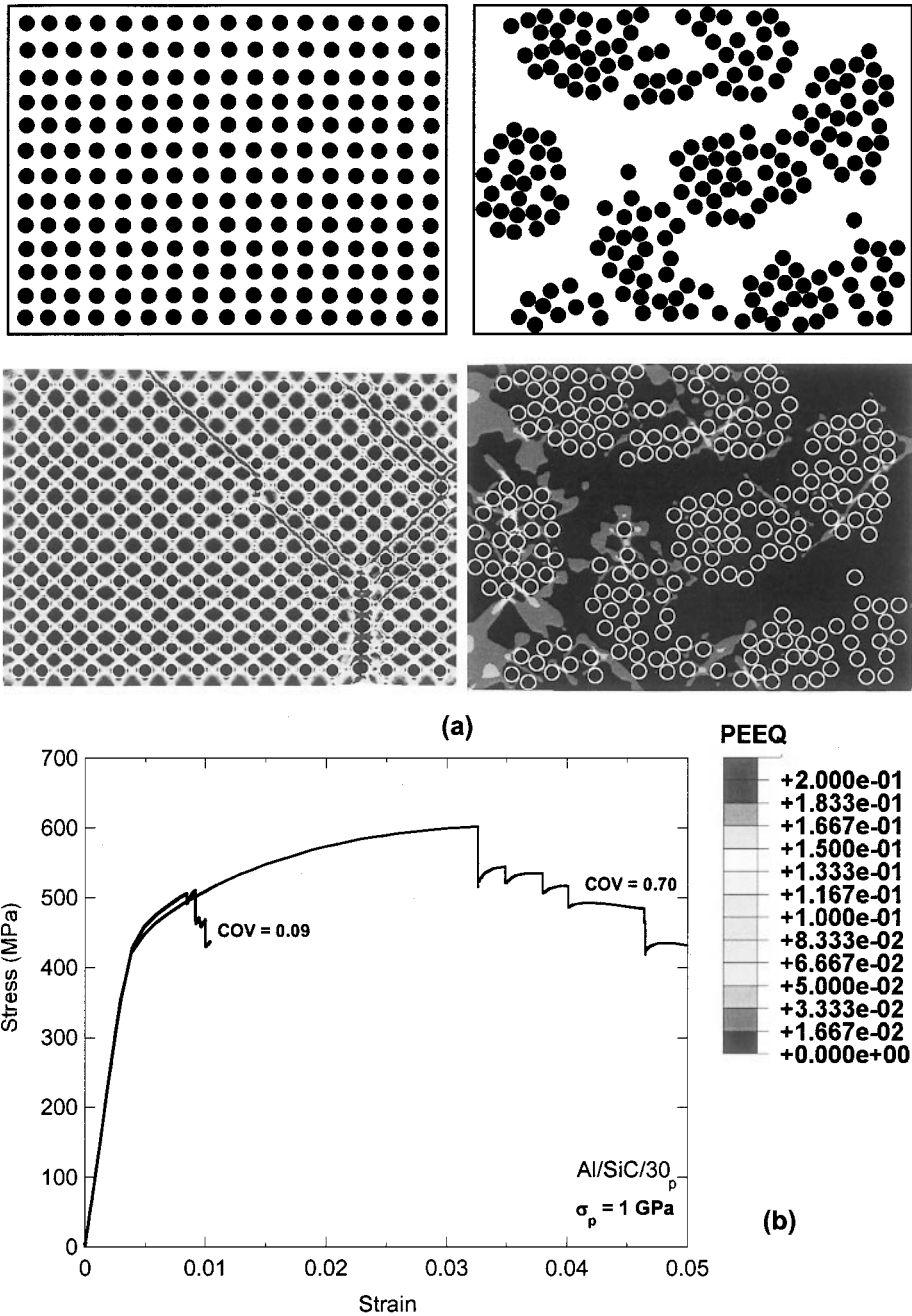
**Fig 7.41** Two-dimensional (2D) finite element analysis of the effect of particle clustering (after Deng and Chawla, 2005): (a) model microstructures consisting of circular SiC particles in Al, showing particle fracture within the cluster and (b) Predicted tensile stress-strain behavior; all particles were assumed to have a strength of 1 GPa. The clustered microstructure has a lower "ductility."
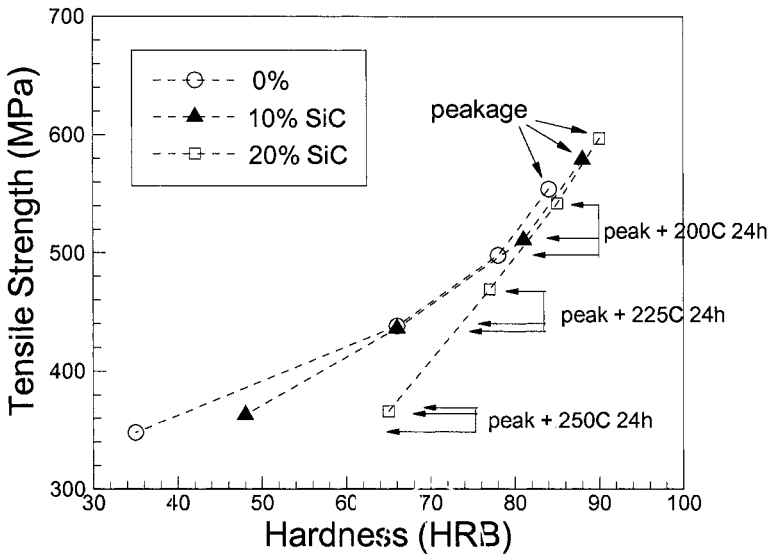
Fig. 7.42 Correlation between macro-hardness and tensile properties of particle-reinforced MMCs (after Shen et al., 2001). Unlike most monolithic metals and alloys, hardness does not necessarily scale with strength of MMCs.
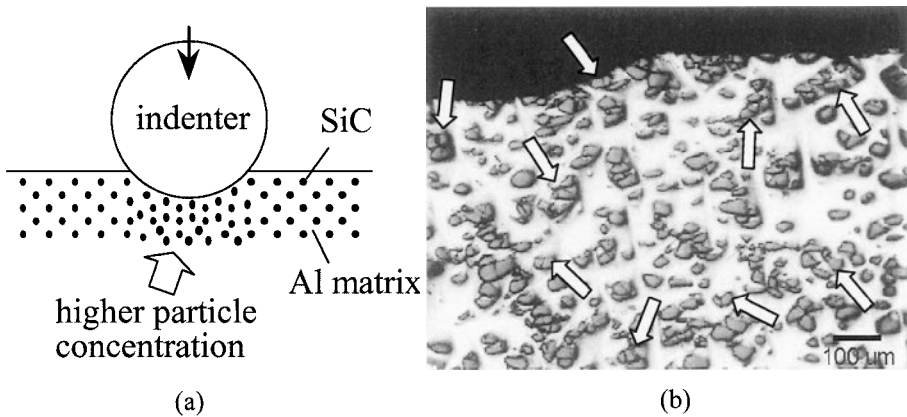
Fig. 7.43 Deformation behavior of particle reinforced MMCs during microindentation (after Shen and Chawla, 2001): (a) localized increase in particle concentration due to plastic flow of the matrix and (b) localized particle fracture, indicated by the arrows.

**(a)**   **(b)**
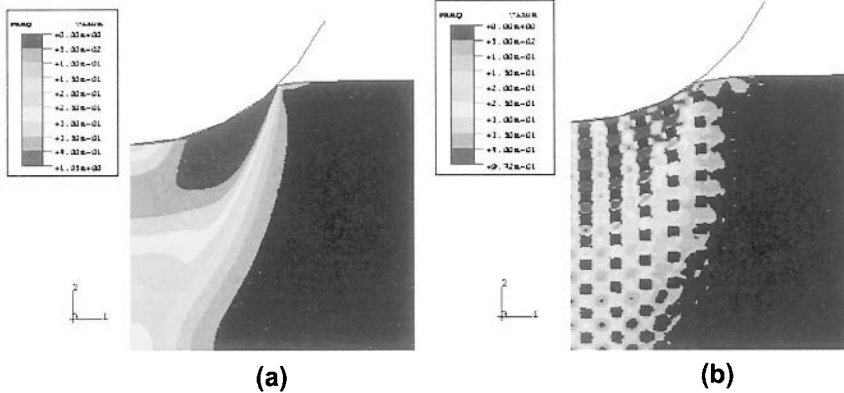
Fig. 7.44 Finite element model of indentation in (a) homogeneous material and (b) particle reinforced composite. In the model, both materials had the same macroscopic tensile constitutive behavior (after Shen et al., 2001). Under indentation, the material system with discrete particles exhibited a higher resistance to deformation.

7.4 FRACTURE TOUGHNESS

The fracture toughness of particle reinforced MMCs is controlled by several factors. These include: (a) volume fraction of reinforcement, (b) interparticle spacing and strength of particles, (c) spatial distribution of particles (i.e., particle clustering), and (d) microstructure of matrix and interface region (as controlled by heat-treatment in age-hardenable alloys). Figure 7.45 is a compilation of toughness in several composite systems, as a function of reinforcement volume fraction (Manoharan et al., 1993, Hunt et al., 1993, and Beck Tan et al., 1994). Note that all the composites show a decrease in toughness with increasing volume fraction of reinforcement. The toughness appears to reach a "plateau" at volume fractions of 20% and above. The decrease in toughness, shown in above, can be explained by an increase in stress triaxiality with increasing volume fraction of particles (similar to what takes place during tensile loading of the composite).

The effect of particle size is less clear-cut. This is because decreasing particle size results in a lower interparticle spacing. In addition, it also results in an increase in strength of ceramic particle, because of a lower probability of encountering a strength-limiting flaw. It has been shown that the degree of clustering increases with decreasing particle size (Hunt et al., 1993), and that the degree of indirect strengthening increases with
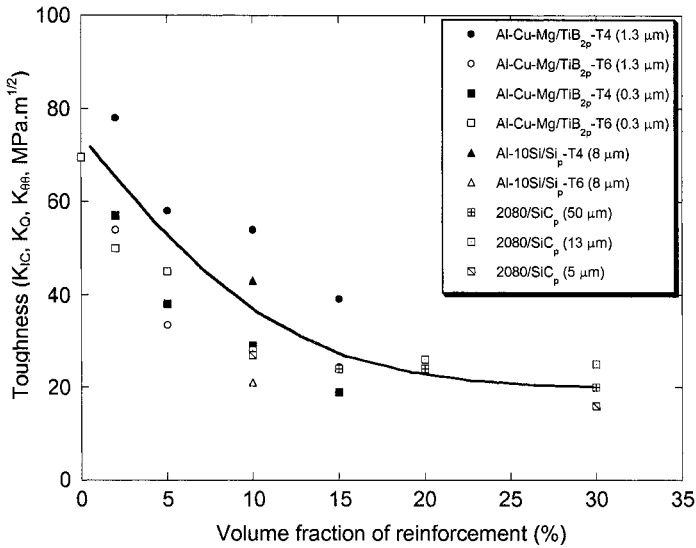
Figure 7.45 Toughness of several particle reinforced MMCs as a function of reinforcement volume fraction (after Manoharan et al., 1993, Hunt et al., 1993, and Beck Tan et al., 1994). All the composites show a decrease in toughness with increasing volume fraction, reaching a "plateau" at volume fraction of about 20% and above.
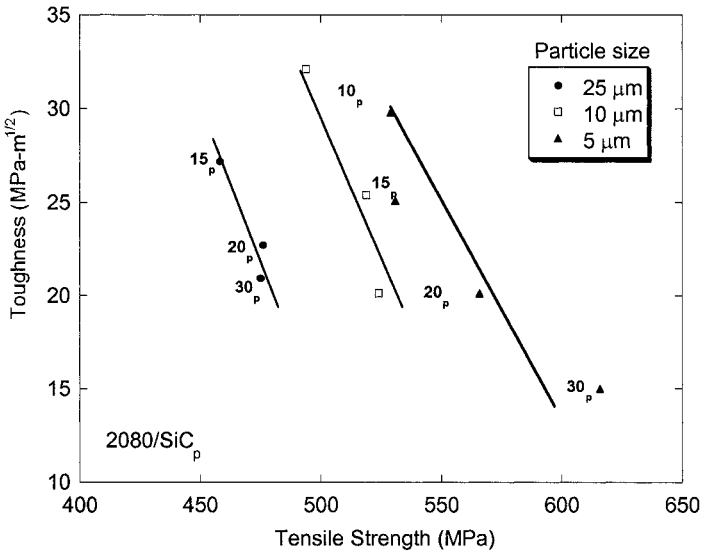

Figure 7.46 Effect of particle size on toughness of a $2080/SiC_p$ composite, at three volume fractions (after Hunt et al., 1993). For a given volume fraction, the toughness of the composite decreases slightly with decreasing particle size.

decreasing particle size (Arsenault and Shi, 1986). Figure 7.46 shows the decrease in toughness of a 2080/SiC$_p$ composite with increasing strength, at three volume fractions and as a function of particle size. The curve for the largest particle size is farthest left, because of the decrease in the strength of the composite with increasing particle size. It is interesting to note that, for a given volume fraction, the toughness of the composite decreases slightly with decreasing particle size. The effect of particle size on toughness was also investigated by Kamat et al. (1989). They studied the fracture toughness behavior of Al$_2$O$_3$ particle reinforced Al matrix composites at volume fractions of 10 and 20% Al$_2$O$_3$, and several particle sizes ranging between 5 and 50 μm. At large particle sizes (> 15 μm), particle fracture was hypothesized to cause unstable crack growth and much lower crack growth toughness. At smaller particle diameter, interfacial decohesion took place. In this lower particle size (and lower interparticle spacing) regime, the behavior of the composites was found to follow the model of Rice and Johnson, where particle/matrix decohesion is assumed to take place at the interface ahead of the main crack. The coalescence of voids arising from particle/matrix decohesion is facilitated by a decrease in interparticle spacing. Their model showed the ratio of toughness-to-fracture strength, J$_{Ic}$/σ$_f$, to be directly proportional to the interparticle diameter, λ:

$$\frac{J_{Ic}}{\sigma_f} = \lambda$$

The fracture toughness is also influenced by the degree of clustering of particles. Lloyd (1995) obtained varying degrees of clustering by varying the cooling rate of a cast A356/SiC/15$_p$ composite, Fig. 7.47. As mentioned in Chapter 4, faster cooling rates result in less time for particle pushing from dendrites, resulting in a more homogeneous distribution of particles. This work clearly shows that with increasing clustering (quantified by an increase in minimum edge-to-edge spacing of particles), the toughness decreases. This stems from an increase in stress triaxiality caused by particle clusters. The toughness is also very much affected by matrix microstructure. Manoharan and Lewandowski (1990) studied the fracture toughness behavior of SiC particle reinforced Al matrix composites, Fig. 7.48. The materials were heat treated to the underaged and overaged condition and had the same nominal tensile strength. The fracture toughness in the two heat treated conditions was quite different. In the UA condition the toughness was twice as large as that of the OA material. This was attributed to a transition in fracture mode from particle-fracture controlled (UA) to interfacial decohesion (OA). The ease of interfacial decohesion was explained by coarsening of precipitates and weakening at the particle/matrix
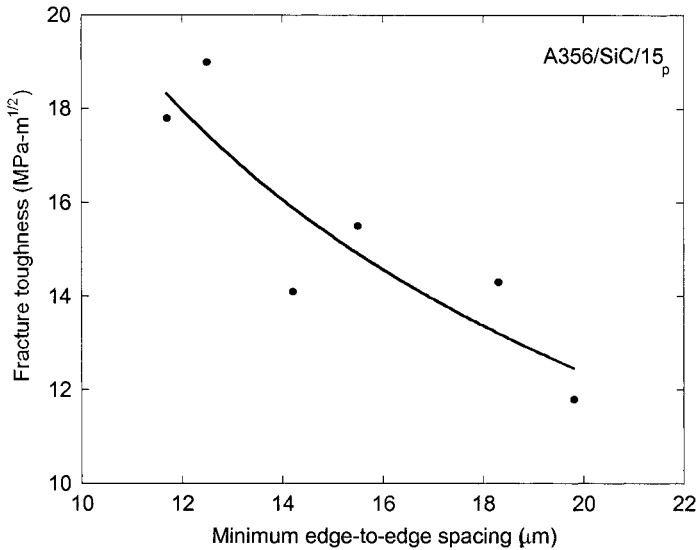
Fig. 7.47 Effect of particle clustering on toughness of a cast A356/SiC/15$_p$ composite (after Lloyd, 1995). With increasing clustering (quantified by minimum edge-to-edge spacing of the particles), the toughness decreases.
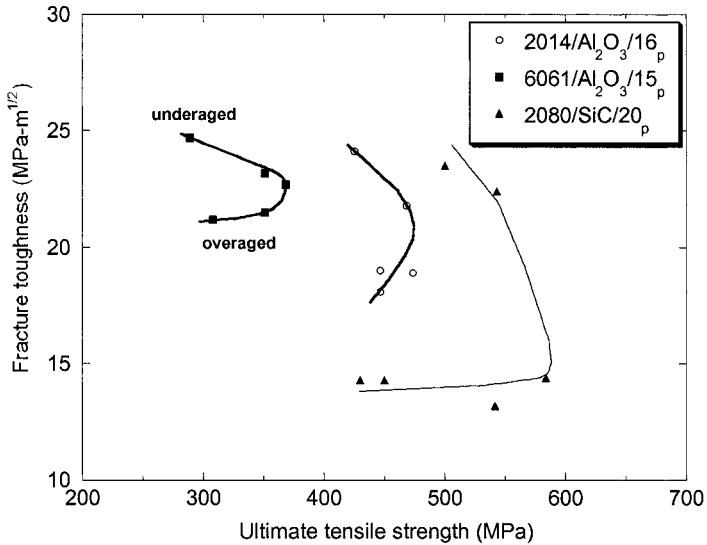
Fig. 7.48 Effect of matrix microstructure on the fracture toughness-tensile strength relationship in particle reinforced MMCs (after Lewandowski, 2000; Hunt et al.; 1993, Kamat et al., 1989). For a given tensile strength, the toughness is higher in the underaged condition vis-à-vis the overaged condition.
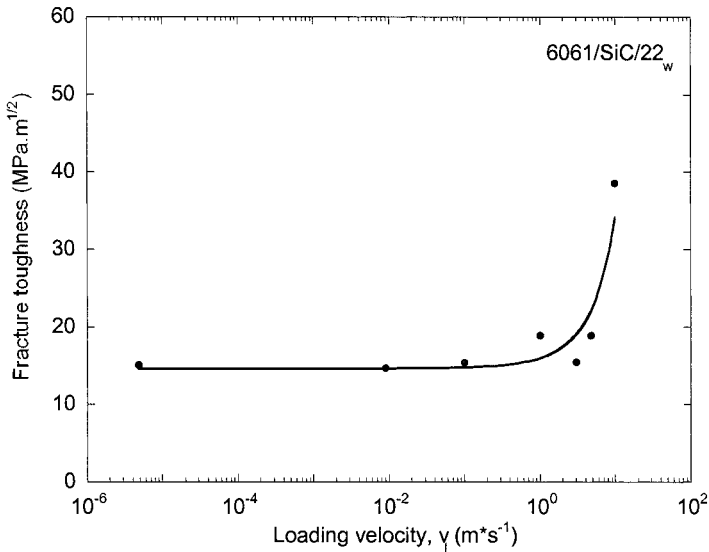
Fig. 7.49 Effect of loading velocity on the fracture toughness of a 6061/SiC/22$_w$ (after Wang and Kobayashi, 1997). Above a loading velocity of 10 m/s, the fracture toughness increased significantly.

interface. In the unreinforced alloy the toughness in both UA and OA conditions was similar.

The toughness of particle reinforced MMCs has also been shown to be a function of loading velocity. Wang and Kobayashi (1997) examined the effect of loading velocity on the fracture toughness of a 6061/SiC/22$_w$, Fig. 7.49. At a loading velocity above 10 m/s, the fracture toughness increased significantly. Fractographic analysis showed that matrix dimples were deeper and the damage zone extended to a longer distance at the faster loading rate. It was postulated that the very fast loading rate did not allow enough time for interaction and coalescence between cracks and voids.

References

Arsenault, R.J., and N. Shi, (1986) *Mater. Sci. Eng.*, **81**, 175.

Ayyar, A., J.J. Williams, and N. Chawla, (2005) *Comp. Sci. Tech.*, submitted.

Beck Tan, N.C., R.M. Aikin, Jr., and R.M. Briber, (1994) *Metall. Mater. Trans.*, **25A**, 2461-2468.

Blucher, J.T., U. Narusawa, M. Katsumata, and A. Nemeth, (2001) *Composites*, **32**, 1759-1766.

Boehlert, C.J., B.S. Majumdar, S. Krishnamurty, and D.B. Miracle, (1997) *Metall. Mater. Trans.*, **28A**, 309-323.

Brockenbrough, J.R., S. Suresh, and H.A. Wienecke, (1991) *Acta Metall. Mater.*, **39**, 735-752.

Bushby, R.S., (1998) *Mater. Sci. Tech.*, **14**, 877-886.

Chan, K.S., (1993) *Metall. Trans.*, **24A**, 1531-1542.

Chawla, K.K., (1973a) *Phil. Mag.*, **28**, 401.

Chawla, K.K., (1973b) *Metallography*, **6**, 155-169.

Chawla, K.K., (1998) *Composite Materials - Science and Engineering*, 2nd Ed., Springer-Verlag, New York, p. 102.

Chawla, K.K., and M. Metzger, (1972) *J. Mater. Sci.*, **7**, 34.

Chawla, N., C. Andres, J.W. Jones, and J.E. Allison, (1998a) *Metall. Mater. Trans.*, **29A**, 2843.

Chawla, N., C. Andres, J.W. Jones, and J.E. Allison, (1998b) *Scripta Mater.*, **38**, 1596.

Chawla, N., U. Habel, Y.-L. Shen, C. Andres, J.W. Jones, and J.E. Allison, (2000) *Metall. Mater. Trans.*, **31A**, 531-540.

Chawla, N., and Y.-L. Shen, (2001) *Adv. Eng. Mater.*, **3**, 357-370.

Chawla, N., J.J. Williams, and R. Saha, (2002a) *J. Light Metals*, **2**, 215-227.

Chawla, N., J.J. Williams, and R. Saha, (2002b) *Metall. Trans.*, **33A**, 3861-3869.

Chawla, N., B.V. Patel, M. Koopman, K.K. Chawla, E.R. Fuller, B.R. Patterson, and S. Langer, (2003) *Mater. Charac.*, **49**, 395-407.

Chawla, N., V.V. Ganesh, and B. Wunsch, (2004) *Scripta Mater.*, **51**, 161-165.

Cheskis, H.P., and R.W. Heckel, (1970) *Metall. Trans.*, **1**, 1931-1942.

Christman, T., A. Needleman and S. Suresh, (1989) *Acta Metall. Mater.*, **37**, 3029.

Cook, J., and J.E. Gordon, (1964) *Proc. Roy. Soc. London*, **A228**, 508.

Corbin, S.F. and D.S. Wilkinson, (1994) *Acta Metall. Mater.*, **42**, 1319.

Cornie, J.A., M.L. Seleznev, M. Ralph, and F.A. Armatis, (1993) *Mater. Sci. Eng.*, **A162**, 135-142.

Cox, B.N., (1990) *Acta Metall. Mater.*, **38**, 2411.

Cox, H.L., (1952) *Brit. J. App. Phys.*, **3**, 122.

Curtin, W.A., (1993) *Composites*, **24** 98-102.

Davis, L.C., and J.E. Allison, (1993) *Metall. Trans.*, **24A**, 2487.

Deng, X., and N. Chawla, (2005) *J. Mater. Sci.*, submitted.

Deve´, H.E., (1997) *Acta Mater.*, **45**, 5041-5046.

Deve´, H.E., and C. McCullough, (1995) *JOM*, **7**, 33-37.

Dirichlet, G.L., (1850) *J. Reine Angew. Math.*, **40**, 209-227.

Dunand, D.C., and A. Mortensen, (1991) *Acta Metall. Mater.*, **39**, 1417-1429.

Dutta, I., J.D. Sims and D.M. Seigenthaler, (1993) *Acta Metall. Mater.*, **41**, 885.

Eldridge, J.I., D.R. Wheeler, R.R. Bowman, and A. Korenyi-Both, (1997) *J. Mater. Res.*, **12**, 2191-2197.

Evans, A.G., and D.B. Marshall, (1989) *Acta Metall.*, **37**, 2567.

Faucon, A., T. Lorriot, E. Martin, S. Auvray, Y. Lepetitcorps, K. Dyos, and R.A. Shatwell, (2001) *Comp. Sci. Tech.*, **61**, 347-354.

Galvez, F., C. Gonzalez, P. Poza, and J. LLorca, (2001) *Scripta Mater.*, **44**, 2667-2671.

Ganesh, V.V., and N. Chawla, (2004) *Metall. Mater. Trans.*, **35A**, 53-62.

Ganesh, V.V., and N. Chawla, (2005) *Mater. Sci. Eng.*, **A391**, 342-353.

Gao, Y.C., Y.W. Mai, and B. Cotterell, (1988) *SAMPE*, **39**, 550.

Gonzalez, C., and J. LLorca, (2001) *Acta Mater.*, **49**, 3505-3519.

Goodier, J.N., (1933) *J. Appl. Mech.*, **55-7**, 39.

Grimes, H.H., R.A. Lad, and J.E. Maisel, (1977) *Metall. Trans.*, **8**, 1999-2005.

Guden, M., and I.W. Hall, (2000) *Computers and Struc.*, **76**, 139-144.

Gupta, V., (1991) *MRS Bull.*, **16** (No. 4), 39.

Gupta, V., J. Yuan, and D. Martinez, (1993) *J. Amer. Ceram. Soc.*, **76**, 305.

Hack, J.E., R.A. Page, and G.R. Leverant, (1984) *Metall. Trans.*, **15A**, 1389-1396.

He, M.Y., and J.W. Hutchinson, (1989) *J. App. Mech.*, **56**, 270.

Humphreys, F.J., (1977) *Acta Metall.*, **25** 1323-1344.

Humphreys, F.J., (1991) *Mater. Sci. Eng.*, **135A,** 267-273.

Hunt, W.H., T.M. Osman, and J.J. Lewandowski, (1993) *JOM*, **45**, 30-35.

Hutchinson, J.W., and H.M. Jensen, (1990) *Mech. Matls.*, **9**, 139-163.

Isaacs, J.A., and A. Mortensen, (1992) *Metall. Trans.*, **23A**, 1207-1219.

Jansson, S., H.E. Deve, and A.G. Evans, (1991) *Metall. Mater. Trans.*, **22A**, 2975.

Jeong, H., D.K. Hsu, R.E. Shannon, P.K. Liaw, (1994) *Metall. Mater. Trans.*, **25A**, 799-809.

Kamat, S., J.P. Hirth, and R. Mehrabian, (1989) *Acta Metall.*, **37**, 2395.

Kelly, A., (1973) *Strong Solids*, Clarendon Press, Oxford, p. 157.

Kelly, A., and H. Lilholt, (1969) *Phil. Mag.*, **20**, 311-328.

Kerans, R.J., and T.A. Parthasarathy, (1991) *J. Am. Ceram. Soc.*, **74**, 1585-1596.

Krajewski, P.E., J.E. Allison, and J.W. Jones, (1993) *Metall. Mater. Trans.*, **24**, 2731.

Konitzer, D.G., and M.H. Loretto, (1989) *Mater. Sci. Eng.*, **A107**, 217-223.

Kyono, T., I.W. Hall, and M. Taya, (1986) *J. Mater. Sci.*, **21**, 4269-4280.

Levy, A., and J. M. Papazian, (1991) *Acta Metall. Mater.*, **39**, 2255.

Lewandowski, J.J., (2000) in *Comprehensive Composite Materials*, T.W. Clyne, A. Kelly, and C. Zweben (eds.), Elsevier, vol. 3, pp. 151-187.

Lewandowski, J.J., D.S. Liu, and C. Liu, (1991) *Scripta Metall.*, **25**, 21.

Leyens, C., J. Hausmann, and J. Kumpfert, (2003) *Adv. Eng. Mater.*, **5**, 399-410.

LLorca, J., (1995) *Acta Metall. Mater.*, **43**, 181-192.

LLorca, J., A. Needleman and S. Suresh, (1991) *Acta Metall. Mater*, **39**, 2317.

Lloyd, D.J., (1995) in *Intrinsic and Extrinsic Fracture Mechanisms in Inorganic Composite Systems*, J.J. Lewandowski and W.H. Hunt (eds.), TMS-AIME, Warrendale, PA, pp. 39-47.

Lloyd, D.J., (1997) in *Composites Engineering Handbook* (P.K. Mallick, ed.), Marcel Dekker, New York, pp. 631-669.

Logsdon, W.A., and P.K. Liaw, (1986) *Eng. Frac. Mech.*, **24**, 737-751.

Manoharan, M., and J.J. Lewandowski, (1990) *Acta Metall. Mater.*, **38**, 489-496.

Manoharan, M., and J.J. Lewandowski, (1992) *Mater. Sci. Eng.*, **A150**, 179-186.

Manoharan, M., J.J. Lewandowski, and W.H. Hunt, (1993) *Mater. Sci. Eng.*, **A172**, 63-69.

Meyers, M.A., and K.K. Chawla, (1999) *Mechanical Behavior of Materials*, Prentice-Hall, Upper Saddle River, NJ, p. 493.

Miller, D.A., and D.C. Lagoudas, (2000) *J. Eng. Mater. Tech.*, **122**, 74-79.

Mikata, Y., and M. Taya, (1985) *J. Compos. Mater.*, **19**, 554.

McCullough, C., H.E. Devé, and T.E. Channel, (1994) *Mater. Sci. Eng.*, **A189**, 147-154.

Mummery, P.M., B. Derby, D.J. Buttle, and C.B. Scruby, (1991) in *Proc. of Euromat 91*, T.W. Clyne and P.J. Withers (eds.), vol. 2, Cambridge, UK, pp. 441-447.

Murphy, A.M., S.J. Howard, and T.W. Clyne, (1998) *Mater. Sci. Tech.*, **14**, 959-968.

Nardone, V.C., and K.M. Prewo, (1986) *Scripta Metall.*, **23**, 291.

Page, R.A., J.E. Hack, R. Sherman, and G.R. Leverant, (1984) *Metall. Trans.*, **15A**, 1397-1405.

Rao, K.T. Venkateshwara, S.C. Siu, and R.O. Ritchie, (1993) *Metall. Trans.*, **24A**, 721-734

Rosenberger, A.H., P.R. Smith, and S.M. Russ, (1999) *J. Comp. Tech. Res.*, **21**, 164-172.

Rossoll, A., B. Moser, and A. Mortensen, (2005) *Mech. Mater.*, **37**, 1.

Ruhle, M., and A.G. Evans, (1988) *Mater. Sci. Eng.*, **A107**, 187.

Segurado, J., C. Gonzalez, and J. LLorca, (2003) *Acta Mater.*, **51**, 2355-2369.

Shen, Y.-L., and N. Chawla, (2001) *Mater. Sci. Eng.*, **A297**, 44-47.

Shen, Y.-L., M. Finot, A. Needleman, and S. Suresh, (1994) *Acta Metall. Mater.*, **42**, 77.

Shen, Y.-L., M. Finot, A. Needleman, and S. Suresh, (1995) *Acta Metall. Mater.*, **43**, 1701.

Shen, Y.-L., J.J. Williams, G. Piotrowski, N. Chawla, and Y.L. Guo, (2001) *Acta Mater.*, **49**, 3219-3229.

Schulte, K., and K. Minoshima, (1993) *Composites*, **24**, 197-208.

Shetty, D.K., (1988) *J. Amer. Ceram. Soc.*, **71**, C-107.

Steglich, D., T. Siegmund, and W. Brocks, (1999) *Comput. Mater. Sci.*, **16**, 404-413.

Suresh, S., and K.K. Chawla, (1993) in *Fundamentals of Metal Matrix Composites*, Suresh, S., A. Mortensen, and A. Needleman, eds., Butterworth-Heinemann, Stoneham, MA, p. 119.

Termonia, Y., (1987) *J. Mater. Sci.*, **22**, 504-508.

Toda, H., T. Gouda, and T. Kobayashi, (1998) *Mater. Sci. Tech.*, **14**, 925-932.

Torquato, S., (2002) *Random Heterogeneous Materials: Microstructure and Macroscopic Properties*, Springer-Verlag, New York, pp. 160–176.

Vogelsang, M., R.J. Arsenault, and R.M. Fisher, (1986) *Metall. Trans.*, **17A**, 379.

Voleti, S.R., C.R. Ananth, and N. Chandra, (1998) *J. Comp. Tech. Res.*, **29**, 203-209.

Wang, L., and T. Kobayashi, (1997) *Mater. Trans. JIM.*, **38**, 615-621.

Warrier, S.G., and B.S. Majumdar, (1997) *Mater. Sci. Eng.*, **237**, 256-257.

Young, R.J., (1994) in *High Performance Composites: Commonalty of Phenomena*, K.K. Chawla, P.K. Liaw, and S.G. Fishman, eds., TMS, Warrendale, PA, p. 263.